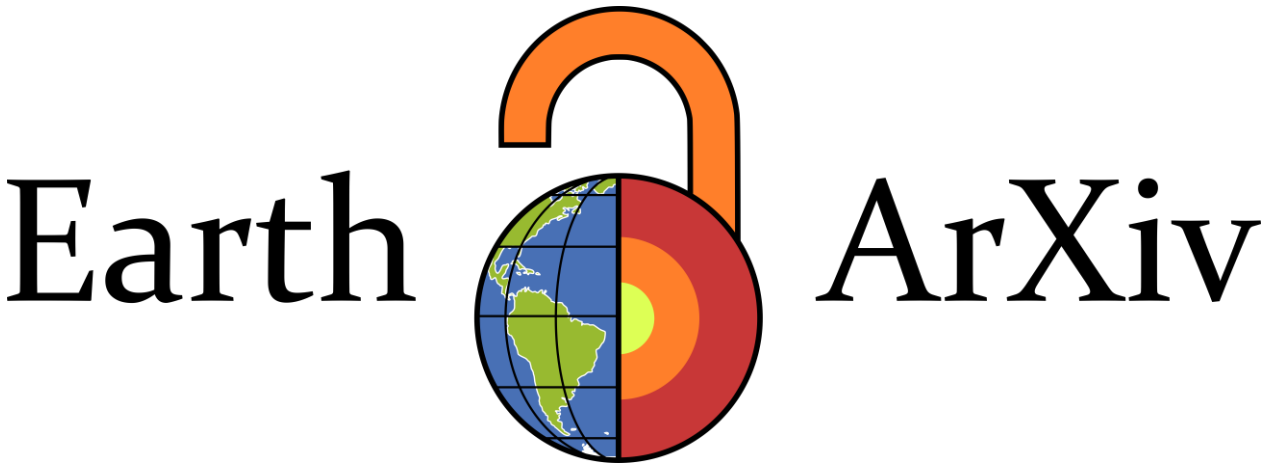

This is a non-peer-reviewed preprint submitted to EarthArXiv.

This manuscript has been submitted for publication. Please note the manuscript has yet to be formally accepted for publication. Subsequent versions of this manuscript may have slightly different content. If accepted, the final version of this manuscript will be available via the 'Peer-reviewed Publication DOI' link on the right-hand side of this webpage. Please feel free to contact any of the authors; we welcome feedback.

Beyond calcite: Crude-urease EICP reveals metal-specific crystallogenetic pathways

Dickinson, Heloisa[a]; MacDonald, John[a]; Toney, Jaime L.[a]
[a]School of Geographical and Earth Sciences, University of Glasgow

---

Abstract

Enzyme-induced carbonate precipitation (EICP) has emerged as a versatile approach for soil improvement and contaminant immobilisation, yet performance is commonly evaluated from bulk metal removal efficiency while the mineralogical fate of retained metals remains poorly understood. Here, Pb, Co and Cr are compared under identical urease-driven EICP conditions using a crude soybean-derived urease extract, with metal retention pathways resolved through SEM–EDS, powder X-ray diffraction with Rietveld refinement, FTIR spectroscopy and chemical-field imaging/μXRF mapping. Across all treatments (2–20 mM), Pb and Co amended systems maintained high alkalinity (final pH ≈ 8.1–8.2) and high removal efficiencies (>99% for Pb; 97–99% for Co) but exhibited contrasting mineralogical outcomes. Pb showed a concentration-dependent transition from calcite-dominated assemblages to progressive stabilisation of a discrete Pb-carbonate population: cerussite was absent at low Pb, emerged at intermediate loading (~3 wt%) and increased at high loading (~6 wt%), coexisting with $CaCO_3$ domains bearing low Pb association and intra-particle chemical zoning. In contrast, Co remained associated with calcite-dominated products across all concentrations, with no evidence for a discrete cobalt carbonate phase; Co occurs at low wt% levels distributed diffusely within $CaCO_3$-rich domains. Chromium displayed the strongest divergence from carbonate-dominated behaviour. Increasing Cr loading reduced ureolysis, precipitate mass (to ~0.5 g at 20 mM) and removal efficiency (to ~87%), and was accompanied by an abrupt transition to abundant elongated prismatic morphologies. SEM–EDS identifies chemically discrete Cr-rich, Ca-poor domains together with Ca–S-rich precipitates exhibiting gypsum-like habits, indicating a shift from carbonate-controlled mineralisation towards sulphate-associated retention pathways at high loading. Together, these results demonstrate that under otherwise identical crude-enzyme EICP conditions, metal identity redirects carbonate biomineralization into distinct crystallogenetic pathways, with direct implications for predicting immobilisation mechanisms and remediation design.

---

1. Introduction

Carbonate biomineralization is a fundamental geochemical process that shapes marine sediments, soils and freshwater systems and underpins a wide range of biologically mediated mineral formation pathways (Lowenstam & Weiner, 1989; Dove et al., 2003; Weiner & Addadi, 2011). Harnessing these processes in engineered settings

has led to the development of enzyme-induced carbonate precipitation (EICP), in which urease-driven reactions promote rapid carbonate supersaturation and $CaCO_3$ formation under ambient conditions. As a result, EICP has been increasingly applied in biocementation, soil improvement, contaminant immobilisation, and carbonate-based carbon sequestration (DeJong et al., 2006; Whiffin et al., 2007; Hamdan & Kavazanjian, 2016; Neupane et al., 2015).

Despite its growing use, EICP-based remediation strategies are still largely evaluated in terms of bulk metal removal efficiency, while the mineralogical fate of immobilised metals remains poorly constrained. Carbonate precipitation is commonly treated as a uniform process, implicitly assuming that metals retained during EICP are stabilised through equivalent mechanisms and exhibit comparable long-term behaviour. However, extensive experimental and theoretical work on carbonate systems demonstrates that metals may follow fundamentally different crystallogenetic pathways during precipitation, leading to contrasting modes of retention, stability, and susceptibility to remobilisation (McBride, 1980; Reeder, 1996; Stipp et al., 1992).

Resolving the mineralogical controls on metal partitioning is therefore critical for developing predictive carbonate-based remediation approaches. Different metals interact distinctly with $CaCO_3$-forming systems, influencing nucleation, growth kinetics, phase selection, and crystal chemistry in ways that cannot be inferred from removal efficiency alone (Paquette & Reeder, 1995; Reeder et al., 1999). Without explicit identification of the mineral phases and crystallogenetic contexts in which metals are retained, EICP remains an empirical, system-specific technology with limited capacity for extrapolation across contaminants and environmental conditions.

Pb, Co and Cr provide a particularly instructive framework for addressing this gap, as they span a wide range of crystal-chemical behaviours relevant to carbonate systems. Pb^{2+} exhibits strong surface affinity but limited lattice compatibility with calcite, commonly forming discrete Pb-carbonate phases such as cerussite (Reeder et al., 1999; Sturchio et al., 1997). Co^{2+} is more closely matched to Ca^{2+} in charge and size, yet its incorporation into calcite is energetically constrained and often restricted to defect- and step-controlled growth environments (Lorens, 1981; Paquette & Reeder, 1995). In contrast, Cr(III) is largely incompatible with the calcite lattice and is typically retained via non-substitutional pathways, including surface adsorption and hydroxide- or oxide-associated domains, while also perturbing carbonate crystallisation (García-Sánchez & Alvarez-Ayuso, 2002; Fang et al., 2022).

Despite their relevance to biomineral engineering and environmental remediation, these metals have not been systematically compared under identical enzyme-induced carbonate precipitation conditions. This limits mechanistic understanding of how metal-specific crystallogenetic behaviour governs immobilisation pathways and long-term stability.

In this study, we investigate the crystallogenetic divergence of Pb, Co and Cr during carbonate biomineralization under identical urease-driven EICP conditions using a crude soybean-derived enzyme extract. By combining SEM–EDS, XRD Rietveld refinement, FTIR spectroscopy and chemical-field imaging, we identify the mineral

phases formed and resolve metal immobilisation pathways based on phase association and crystallogenetic context. We demonstrate that under identical EICP conditions, metal identity alone is sufficient to redirect carbonate biomineralization into fundamentally different crystallogenetic pathways, with direct implications for the efficiency and predictability of metal immobilisation.

1.1. Theoretical framework: crystallogenetic controls on metal partitioning during EICP

Enzyme-induced carbonate precipitation (EICP) is fundamentally driven by urease-catalysed urea hydrolysis, which increases pH and carbonate alkalinity and promotes $CaCO_3$ supersaturation under ambient conditions (Nemati & Voordouw, 2003; Whiffin et al., 2007; DeJong et al., 2006). While urease is the primary driver of alkalinity generation, crude enzyme extracts also introduce organic macromolecules and ancillary enzymatic activity (e.g., amylase, catalase) that can modify nucleation environments, growth dynamics, and mineral–solution interactions.

Carbonate precipitation under EICP conditions can proceed through multiple crystallogenetic pathways with contrasting capacities for metal uptake. These include substitutional incorporation within the calcite lattice (McBride, 1980; Reeder, 1996), defect- and step-assisted coprecipitation during crystal growth (Stipp et al., 1992; Paquette & Reeder, 1995), and adsorption at crystal surfaces governed by aqueous speciation and surface complexation reactions (Stumm & Morgan, 1996). Where crystal-chemical compatibility is limited or metal carbonate solubility is low, metals may segregate into discrete carbonate phases or be diverted into non-carbonate secondary minerals such as hydroxides, phosphates, or mixed hydroxy-carbonates (Langmuir, 1997; Bourg & Sposito, 2007).

Three first-order controls constrain metal behaviour during carbonate biomineralization. The first is crystal-chemical compatibility, which governs the energetic feasibility of substitution at Ca^{2+} sites and the extent to which metals can be accommodated within carbonate lattices (Reeder, 1996; Paquette & Reeder, 1995). The second is metal-specific aqueous speciation and hydrolysis behaviour, which influences carbonate availability, competitive precipitation pathways, and sensitivity to redox and pH conditions (Stumm & Morgan, 1996; Langmuir, 1997). The third is interaction with early mineral precursors and active growth surfaces, as transient amorphous or poorly ordered phases, often stabilised by organic components, can exert a strong kinetic control on metal partitioning and persistence within the final mineral assemblage (Lowenstam & Weiner, 1989; Addadi & Weiner, 1992; Beniash et al., 1997).

Within this framework, metal immobilisation during EICP is inherently element-specific and pathway-dependent. Identical bulk reaction conditions may therefore yield similar removal efficiencies while producing fundamentally different mineralogical outcomes and retention mechanisms. Resolving these crystallogenetic controls is essential for assessing the stability, reversibility, and environmental performance of

carbonate-based remediation strategies, particularly in enzyme- and organic-rich systems.

2. Materials and Methods

Full experimental details, instrumental settings, and data-analysis procedures are provided in the Supplementary Material; essential methodological information is summarised below.

2.1. Materials and reagents

Urea (≥99%), calcium chloride dihydrate ($CaCl_2 \cdot 2H_2O$), and all metal salts used to prepare stock solutions (Pb^{2+}, Cu^{2+}, Co^{2+}, Cr^{3+}) were of analytical grade and used as received; deionised water (18.2 MΩ·cm) was used in all experiments.

2.2. Preparation of crude urease extract

The crude urease extract was prepared using an aqueous soybean extraction procedure. 80 grams of whole soybeans were soaked in deionised water, blended to a final volume of 1 L, and allowed to stand overnight at room temperature. The mixture was processed using a masticating juicer (Fridja F900) to separate liquid and solid fractions. Calcium carbonate was then added to the liquid fraction to a final concentration of approximately 0.06 M to promote protein precipitation. After settling for 2h at room temperature, the supernatant was decanted, centrifuged (3700 rpm, 5 min, 4 °C), and filtered using Grade 2 filter paper. Urease activity was quantified using the urea hydrolysis assay described by Whiffin (2004) and averaged 2.66 ± 0.7 mM urea min^{-1}. The crude extract was used immediately following activity measurements to minimise potential loss of enzymatic activity.

2.3. Carbonate biomineralization experiments

Carbonate biomineralization experiments were conducted by mixing equal volumes (83.4 mL each) of crude urease extract (CUE), an aqueous solution containing $CaCl_2$ (1 M) and Pb, Co, or Cr at target concentrations of 2 mM (T1), 5 mM (T2), or 20 mM (T3), and a 1 M urea solution. Each treatment was performed in quintuplicate. The resulting reaction mixtures were aliquoted into 50 mL polypropylene centrifuge tubes and incubated at 25 °C for 72 h under static conditions.

Following incubation, suspensions were left to cure at room temperature for an additional 7 days. After curing, solid phases were recovered by paper filtration, rinsed with ultrapure water, and dried in an oven at 37 °C for 24 h prior to mineralogical characterisation.

2.4. Aqueous chemistry

Supernatant samples were collected for analysis of pH, ammonium, and dissolved metal concentrations. pH was measured using a YSI ProDSS multiparameter probe. Ammonium concentrations were quantified using the salicylate colorimetric method on a SEAL AutoAnalyzer AA3. For dissolved metal analysis, aliquots of the supernatant were acidified to 2% (v/v) HNO_3 and analysed by inductively coupled plasma optical emission spectrometry (ICP-OES; Thermo Scientific iCAP 7000).

2.5. SEM–EDS analysis

Scanning electron microscopy (SEM) analyses were conducted on powdered precipitates to characterise morphology and elemental distribution. For morphological imaging, samples were gently dispersed onto carbon adhesive tabs mounted on aluminium stubs and sputter-coated with a thin Au/Pd layer to minimise charging and enhance secondary-electron contrast.

For chemical analyses, including semi-quantitative energy-dispersive X-ray spectroscopy (EDS) and elemental mapping, separate aliquots of the powdered precipitates were mounted on carbon tabs and coated with conductive carbon to avoid spectral interference from metallic coatings.

EDS data were interpreted semi-quantitatively. Owing to matrix effects, particle orientation and the multiphase nature of the precipitates, absolute quantification was not attempted. Instead, EDS spectra and elemental maps were used to assess relative metal enrichment, identify discrete metal-bearing phases and characterise compositional heterogeneity.

2.6. Powder X-ray diffraction and Rietveld refinement

Powder X-ray diffraction data were acquired using a Malvern Panalytical Empyrean (X-ray Diffraction Laboratory, School of Chemistry, University of Glasgow) multipurpose diffractometer equipped with a Cu sealed-tube X-ray source, multicore iCore/dCore motorised optics, a hybrid monochromator, a focusing mirror, and a PIXcel3D detector, operated in reflection geometry at room temperature. Phase identification and quantitative analysis were performed by Rietveld refinement using Profex (Döbelin & Kleeberg, 2015) interfaced with FullProf. Full details of the instrumental configuration and refinement parameters are provided in the Supplementary Material.

2.7. µXRF elemental mapping

Synchrotron-based micro–X-ray fluorescence (µXRF) elemental mapping analyses of Ca, Co, and Pb were conducted at the Brazilian Synchrotron Light Laboratory to characterise elemental distributions.

3. Results

3.1. System-level geochemical response during EICP

System-level geochemical parameters (pH, ammonium production, precipitate mass, and metal removal efficiency) were first evaluated to establish the evolution of EICP conditions across treatments, prior to metal-specific analysis of immobilisation behaviour and mineralogical pathways.

Ureolysis-driven alkalisation responded differently to Pb^{2+}, Co^{2+} and Cr^{3+} under otherwise identical experimental conditions. In Pb^{2+} amended systems, final pH values remained consistently high (≈8.2) across all metal loadings (T1–T3) and closely matched those of the metal-free control (Fig. 1a). Ammonium concentrations were similarly elevated, typically between ~3,500 and 3,700 ppm (Fig. 1b). Precipitate masses in Pb^{2+} treatments were comparable to the control and varied only slightly with increasing metal concentration (1.78–1.81 g; Fig. 1c). Correspondingly, Pb removal efficiencies remained consistently high (>99%) across all treatments (Fig. 1d).

In Co^{2+}-amended systems, final pH values also remained elevated (≈8.1–8.2) across all loadings, comparable to Pb^{2+} treatments and the control (Fig. 1a). Ammonium production was similarly sustained, with concentrations of ~2,950–3,000 ppm (Fig. 1b). In contrast to Pb^{2+}, Co^{2+} treatments yielded substantially lower precipitate masses than the control, with values of ~0.78–0.79 g at T1 and T2 and a further decrease to ~0.57 g at T3 (Fig. 1c). Despite the reduced solid yield, Co removal efficiencies remained high (97–99%) across all treatments, with no systematic decrease with increasing metal concentration (Fig. 1d).

By contrast, Cr^{3+}-amended systems exhibited lower pH values (≈7.8–8.0) than those observed for Pb^{2+} and Co^{2+} and decreased progressively with increasing Cr loading (Fig. 1a). Ammonium concentrations were markedly reduced (~2,000–2,480 ppm) and declined systematically from T1 to T3 (Fig. 1b). This was accompanied by a strong reduction in precipitate mass, from ~1.7 g at T1 to 1.66 in T2 and ~0.5 g at T3 (Fig. 1c). Despite the reduced solid yield, Cr removal efficiencies remained relatively high (87–97%), although a clear decrease was observed at the highest loading (Fig. 1d).

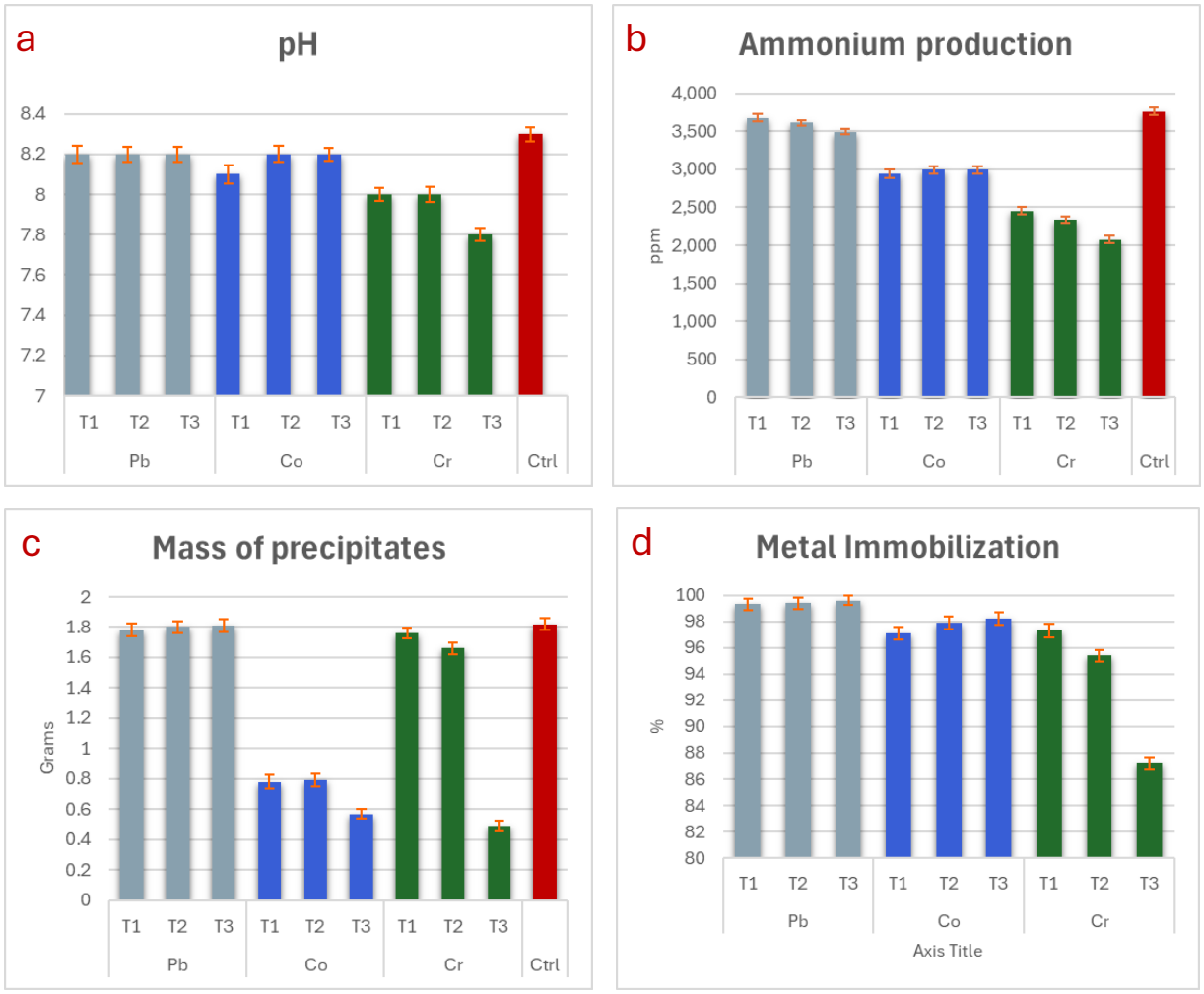

Figure 1. pH (a), ammonium production (b), mass of precipitates (c) and metal immobilisation efficiency (d) measured in crude-enzyme-driven EICP experiments with Pb, Co and Cr at three concentrations (T1–T3), compared with a metal-free control (Ctrl). Values represent mean ± SD (n = 5).

2. Microstructural analysis of precipitates (SEM)

SEM microstructural analyses were performed on powder samples mounted directly onto coated stubs, rather than on polished sections. This approach preserves the native external morphologies of the EICP precipitates and enables clear observation of surface textures and growth features, although aggregates appear in random orientations and may expose only parts of their internal structure. Even so, it provides high-fidelity access to the outer microstructures that characterise each metal treatment. The following subsections describe the principal morphologies observed for Pb, Co and Cr across treatments T1, T2 and T3.

3.2.1. Lead

Pb-treated samples (T1–T3) are dominated by large composite aggregates, typically 40–100 µm in diameter, which constitute the prevailing morphological class across all treatments (Fig 3., Pb-T1, T2 and T3). These aggregates are heterogeneous and comprise multiple intergrown morphotypes rather than a single uniform habit. Common components include truncated sunflower-like structures with shallow central depressions (Fig. 3 Pb A), aggregates of spheres and tabular to platy crystals forming locally grouped domains (Fig. 3 PbT1, T2 and Pb B).

A prominent feature of the Pb system is the occurrence of dense aggregates composed of tightly packed spherical sub-units (fig. 3 Pb-T2 and Pb-D). These coalesced spheroidal clusters are especially abundant and well organised at intermediate Pb loading (T2), forming multi-sphere assemblages with smooth to finely granular surfaces. The surfaces of individual spheres are not uniform, ranging from smooth and compact to finely roughened, nanoparticulate or locally pitted textures, suggesting variable growth and coalescence histories. Individual spheres commonly display shared boundaries and partial fusion. At lower Pb concentration (T1), spheroidal units are present but are less consistently organised and more commonly occur embedded within heterogeneous cauliflower-like aggregates. At the highest loading (T3), spheroidal textures are less regularly expressed and are accompanied by more fragmented and irregular composite masses.

In addition to the $CaCO_3$-dominated aggregates, Pb-treated samples contain a set of morphologies assigned to cerussite that are not observed in the Co or Cr systems. These include fan-like bladed aggregates composed of broad, flattened blades radiating asymmetrically from a core; spherical, raspberry-like globules (typically 2–10 µm in diameter) formed by densely packed nano- to submicron crystallites (Fig. 2 Pb-E); and compact clusters of short, robust prismatic crystals forming blocky intergrown assemblages, most evident in T1. Cerussite-like morphologies commonly occur in close spatial association with spheroidal Pb-bearing aggregates within the same fields of view.

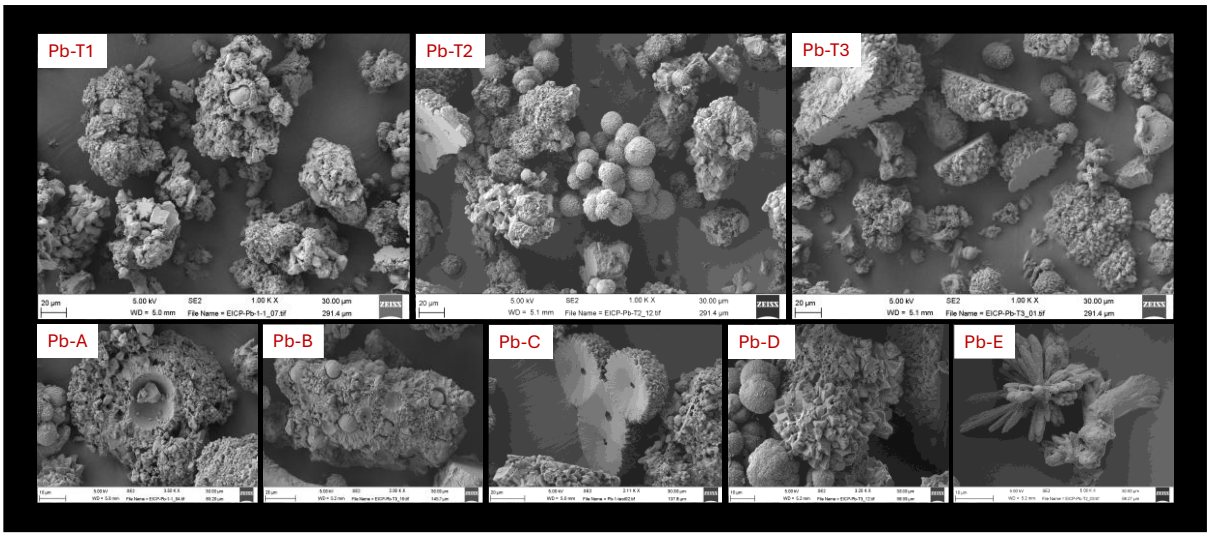

Figure 2. Lead-treated EICP precipitates across treatments (T1–T3) and representative morphologies (Pb-A to Pb-E). SEM images show the dominant Pb-bearing carbonate assemblages formed under increasing Pb loadings. Panels Pb-T1 to Pb-T3 illustrate the progression from loosely aggregated, cauliflower-like clusters (T1) to more compact spheroidal aggregates and botryoidal masses (T2), culminating in heavily fused, irregularly textured precipitates at the highest Pb concentration (T3). Panels Pb-A to Pb-E highlight characteristic Pb-induced morphologies observed throughout the system, including shallow sunflower-like structures with poorly developed radial organisation (Pb-A), botryoidal and nanoparticulate coatings (Pb-B), broad faceted plates and truncated rhombohedra (Pb-C), dense agglomerates with coarse surface textures (Pb-D), and asymmetric cerussite petaloid aggregates (Pb-E). Together, these images illustrate the tendency of Pb^{2+} to disrupt calcite growth, promoting highly aggregated, texturally heterogeneous precipitates across all treatments.

3.2.2. Cobalt

Co-treated samples (T1–T3) exhibit a range of composite precipitate morphologies that vary systematically with treatment level. At T1, the precipitated solids are dominated by irregular composite aggregates, typically ranging from ~20 to 80 µm. At low magnification, these aggregates appear as compact, cauliflower-like masses composed of multiple coalesced sub-units, with domed to lobate outlines and abundant lateral growths. Their surfaces are heterogeneous and micro-roughened, with pervasive fine-scale textural relief (Fig. 4 Co-T1, Co-B).

At T2, the precipitated solids are dominated by porous spherical filigree morphotypes and sunflower-like aggregates, both occurring at smaller sizes than the cauliflower-like aggregates and commonly forming clustered assemblages. The filigree spheres typically appear as well-defined globules with highly open, lace-like surface architectures, whereas the sunflower-like forms consist of compact radial units with short, outward-projecting elements arranged around a central core (Fig. 4 CoT2, Co-F,G,H). These morphotypes frequently occur in close spatial association, with sunflower-like aggregates commonly attached to, or intergrown with, the surfaces of the filigree spheres and grouped into composite clusters (Fig. 4 Co-T2, A).

At T3, the precipitates are dominated by a finer overall granulometry, forming aggregates of spheres with variable surface textures that are commonly associated with a continuous mass and occur as dispersed block-like composites. The spherical units

show heterogeneous surface expression, ranging from roughened coatings to more compact, irregular textures, and are frequently embedded within or partially fused to the surrounding matrix, producing fragmented but cohesive aggregate blocks (Fig. 4 Co-T3, Co-E).

Co-treated samples display a suite of discrete and highly diagnostic microstructures that are unique to the cobalt system. Most distinctive among these are the filigree spheres, which occur as isolated or clustered globules typically 5–20 µm in diameter at T2, but are also observed incipiently at T1 and T3 (Fig. 4 Co-F). These spheres are entirely mantled by an intricate, lace-like nanostructure. At high magnification, their surfaces resolve into tessellated networks of tightly interwoven triangular micro-modules, each composed of short, plate-like crystallites diverging from a central axis and overlapping at slight angular offsets (Fig. 4 Co-G,H).

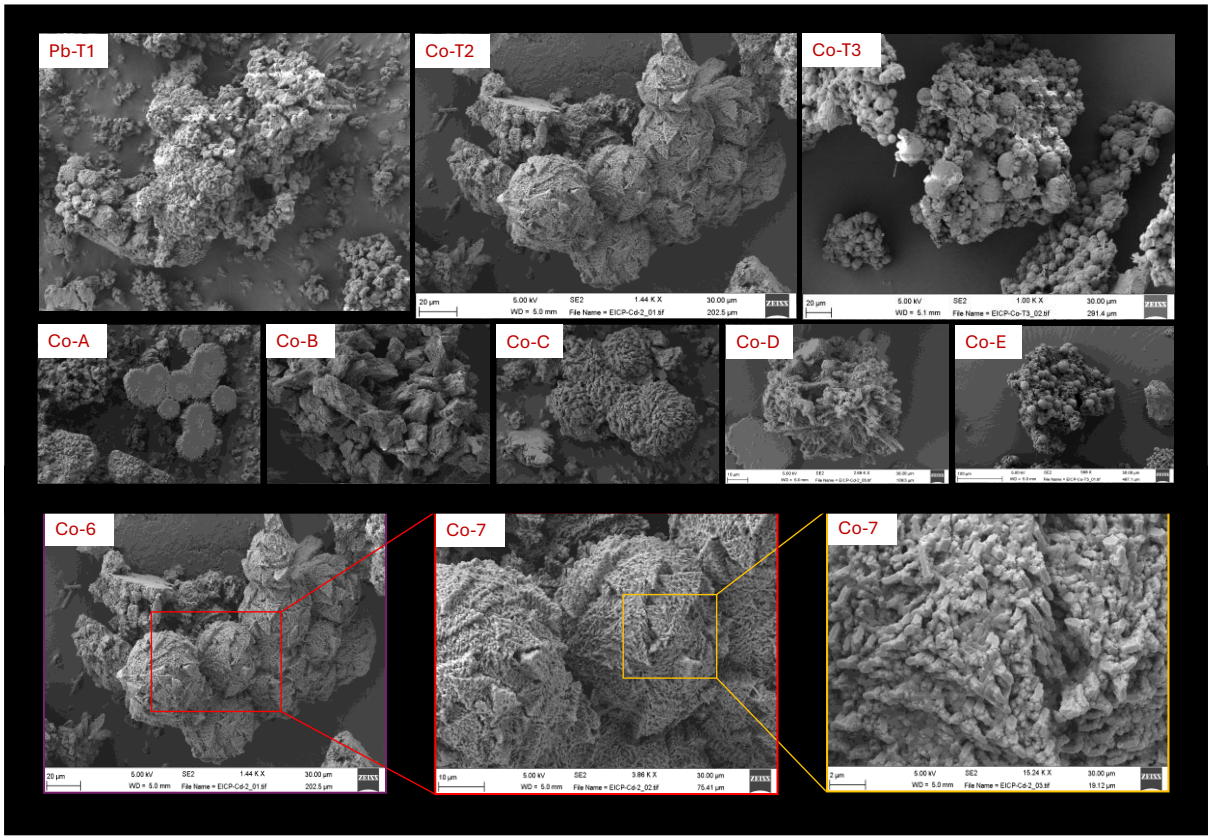

Figure 3. Cobalt-treated EICP precipitates across treatments (T2–T3) with representative morphologies and hierarchical structural detail. SEM images (top row and Co-A to Co-E) show the dominant Co-bearing carbonate aggregates, ranging from compact rosette-like clusters (T2) to densely fused spheroidal masses (T3). Representative morphotypes include multi-petal radial aggregates (Co-A), blocky intergrown plates (Co-B), faceted blades (Co-C), coarse agglomerates (Co-D) and small, tightly packed clusters (Co-E). The second panel (Co-6 and sequential zooms Co-7) highlights the hierarchical organisation of Co-derived structures, revealing tightly interlocked nanoblades and textured surfaces that intensify the radial organisation observed at the particle scale.

3.2.3. Chromium

Cr-treated samples display a clear evolution in precipitate morphology with increasing Cr concentration. At low to intermediate Cr loadings (Fig. 4 Cr-T1, T2), the precipitates are dominated by compact carbonate aggregates, whereas at high loading (Fig. 4 Cr-T3) a distinctly different precipitate population becomes prevalent.

At T1 and T2 (Fig. 4. Cr-T1, T2), the precipitated solids are dominated by compact carbonate aggregates typically 10–70 μm in diameter. These occur as blocky clusters composed of intergrown microcrystals with well-defined faces and sharply delineated aggregate margins. Radial morphologies are common, including sunflower-like particles characterised by broadly circular outlines, shallow central depressions, and rims constructed from densely packed angular sub-units. These radial forms occur both as discrete particles and as components embedded within larger composite aggregates.

Spheroidal to subspheroidal aggregates are additionally observed in T1 and T2 samples. These particles exhibit highly porous, cavernous surfaces and open, shell-like architectures, with perforated margins and locally collapsed interiors. Despite their curved macroscale geometry, their surfaces are composed of angular microcrystalline elements rather than smooth or continuous coatings (Fig. 4 Cr-B, C).

At T3 (Fig 4 Cr-T3, Cr-D, E), the precipitate morphology changes markedly. Carbonate-derived aggregates become less abundant, and the assemblage is instead dominated by fine-grained material together with abundant elongated prismatic crystals forming dense, interwoven mats. These prismatic crystals occur as long, straight to slightly irregular blades, commonly tens of micrometres in length, producing a continuous textural fabric that contrasts with the discrete carbonate aggregates observed at lower Cr loadings. In addition to the prismatic mats, T3 samples contain irregular fine-grained aggregates and smooth, bulbous domains that occur intergrown with the prismatic crystals (Fig. 4 Cr-D, E). Residual carbonate particles are still present but occur primarily as isolated cores or substrates embedded within the fine-grained and prismatic assemblage, rather than as discrete dominant aggregates.

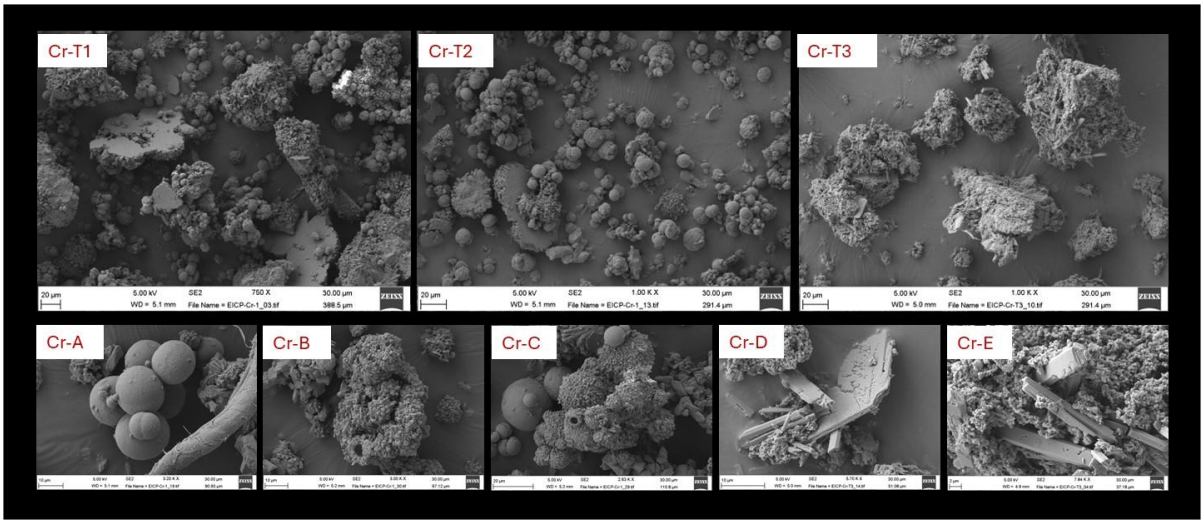

Figure 4. SEM images of Cr-treated EICP precipitates across increasing Cr concentrations (Cr-T1–T3) and representative Cr-associated morphologies (Cr-A to Cr-E). Cr-A shows spheroidal morphotypes commonly observed in T1 and T2. Cr-B and Cr-C illustrate sunflower-like particles and composite aggregate textures characteristic of low to intermediate Cr loadings. Cr-D and Cr-E highlight the abrupt transition toward elongated prismatic morphologies that dominate at T3.

3.2.4. Description of the sunflower-like carbonate texture

Sunflower-like carbonate aggregates are observed across the Pb- and Co-treated systems and at low to intermediate Cr loadings (Cr-T1 and T2 only), occurring in highly variable abundances, and represent a recurrent morphological motif within the EICP precipitates. These structures are characterised by a broadly circular to sub-circular outline, a shallow central depression or concavity, and a peripheral rim composed of radially arranged crystalline sub-units, in a texture that is remarkably similar to a sunflower (Fig. SF1 to SF6).

At the particle scale, sunflower-like aggregates typically range from a few micrometres to a few tens of micrometres in diameter and occur both as discrete particles and as components embedded within larger composite aggregates. The central region commonly appears denser and more compact, whereas the outer rim is defined by outward-projecting elements that impart a radial organisation to the overall morphology.

The radial sub-units forming the rim vary in thickness, length and degree of separation depending on metal treatment and concentration but consistently preserve an organised centre–periphery arrangement. In some cases, these sub-units appear as short, blocky elements, whereas in others they develop as elongated blade-like or plate-like features. The transition between the central core and the radial rim is typically gradual, without sharply defined internal boundaries.

Sunflower-like textures frequently coexist with other carbonate morphologies, including spheroidal aggregates, blocky polyhedral clusters, and prismatic crystals, and are commonly intergrown with or partially overgrown by these forms. Their preservation

ranges from well-defined, symmetric structures to partially disrupted or irregular variants in which the radial organisation is incomplete or locally obscured.

Sunflower-like carbonate aggregates occur in two closely related structural variants. In some particles, the central spheroidal core is preserved *in situ*, forming a compact, smooth to finely textured central body from which radially arranged crystalline sub-units extend outward (Fig. X-A,B). In other cases, the central core is absent or detached, leaving an open central cavity with sharply defined circular to sub-circular margins surrounded by the radial framework (Fig. X-C,D). Intermediate forms are also observed, in which the central core appears partially displaced or fractured but remains strongly associated with the surrounding radial structure. These variants occur within the same samples and commonly coexist with other carbonate morphologies.

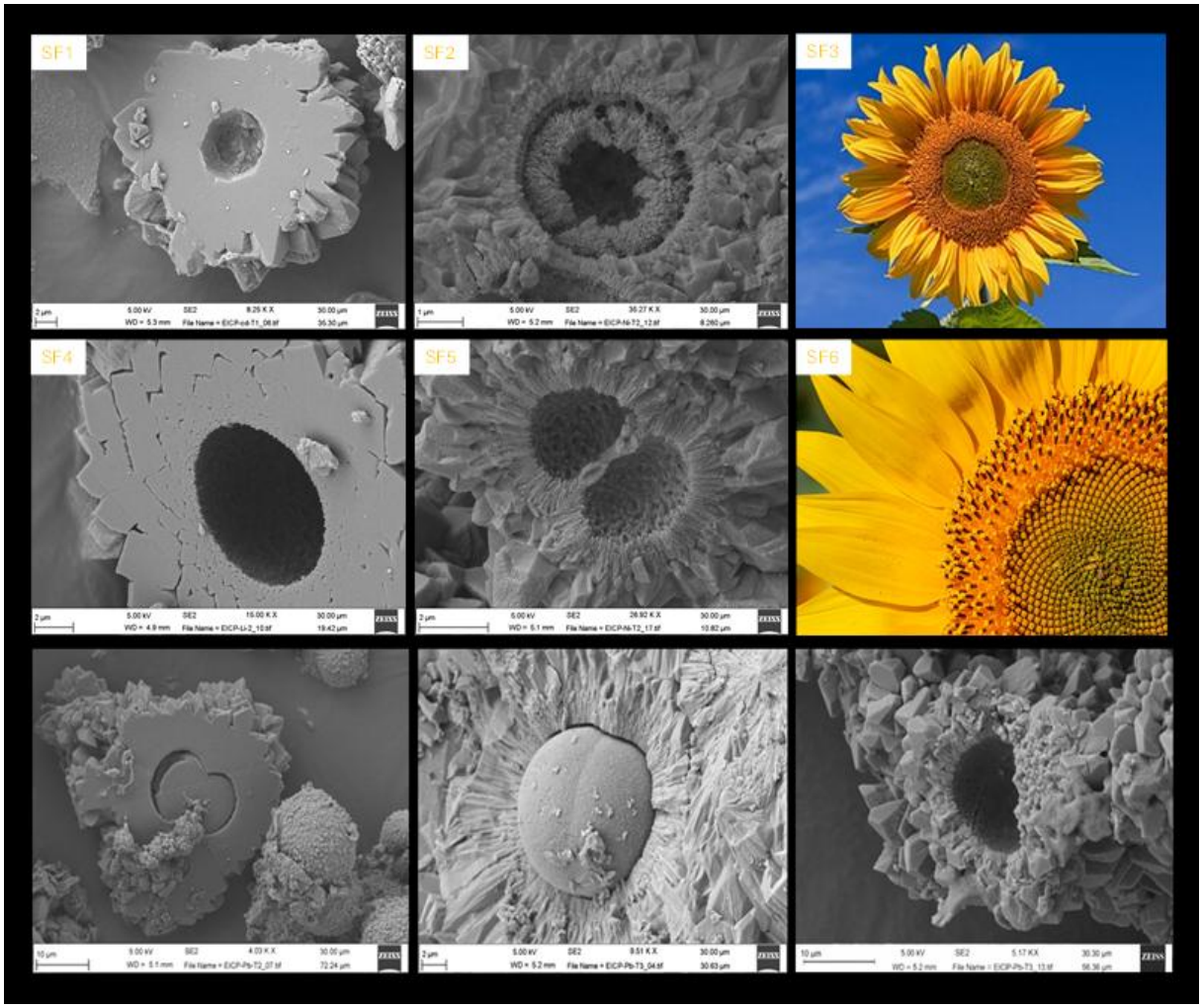

Figure 5. Sunflower-like calcite morphologies formed during metal-doped EICP, shown alongside natural sunflower (common species of *Helianthus*) reference patterns (SF3, SF6). Panels SF1–SF2 and SF4–SF5 show representative SEM images of radial calcite aggregates produced under Pb- and Co-amended conditions. These structures are characterised by a central depression surrounded by outward-radiating crystallites, producing a rosette or "sunflower-like" habit. Pb-rich aggregates (SF1, SF2, SF4) exhibit broader, blocky petals and well-defined central voids, whereas Co-rich structures (SF2, SF5, SF7, SF9) display finer, densely packed radial blades and more pronounced textural organisation. SF8 shows a sunflower pattern with the nucleus preserved.

3.3. Crystalline phase assemblages and phase evolution (PXRD and Rietveld refinement)

Powder X-ray diffraction (PXRD) was used to identify the crystalline phase assemblages associated with the morphologically distinct carbonate precipitates formed under Pb-, Co- and Cr-amended EICP conditions. Particular emphasis is placed on phase evolution across treatments (T1–T3) and on assessing whether the observed diffraction patterns are more consistent with lattice incorporation or with discrete phase precipitation. As no internal standard was employed, phase proportions derived from Rietveld refinement are semi-quantitative and are used here to support comparative mineralogical trends across treatments rather than absolute quantification.

Pb-treated samples exhibited a pronounced concentration-dependent evolution in mineralogical composition. At low Pb concentration (T1), diffraction patterns were dominated by calcite (>98 wt%), with no detectable discrete Pb carbonate phases. At intermediate concentration (T2), weak reflections attributable to cerussite ($PbCO_3$) became discernible, corresponding to ~3 wt% of the crystalline assemblage, alongside an increased contribution from Pb-substituted calcite components. At the highest concentration (T3), cerussite reflections were well defined and intensified, with discrete $PbCO_3$ accounting for ~6 wt% of the precipitate.

Cobalt-treated samples (T1–T3) were dominated by calcite reflections across the entire concentration range, with no distinct peaks attributable to discrete cobalt carbonate phases. Rietveld refinement indicates that the carbonate assemblages are best described by calcite-type components modelled using a range of apparent substitution classes. These classes represent refinement constructs used to capture lattice distortion and compositional heterogeneity rather than true bulk solid-solution compositions. Across all Co treatments, the assemblages therefore remain $CaCO_3$ dominated, with cobalt associated at low and diffuse levels and no evidence for the stabilisation of a discrete Co-rich carbonate phase.

Chromium-treated samples displayed a contrasting mineralogical response to increasing metal loading. At low concentration (T1), diffraction patterns were dominated by calcite and Mg-bearing calcite components, which together comprised the majority of the crystalline assemblage. At intermediate concentration (T2), calcite remained the dominant crystalline phase, accompanied by redistribution among carbonate components. At high concentration (T3), the relative contribution of carbonate reflections decreased markedly. While PXRD indicates a clear departure from a carbonate-dominated crystalline assemblage at this loading, no single alternative non-carbonate crystalline phase could be unequivocally identified from the diffraction data alone. This reflects both the chemical complexity of the Cr-rich precipitates and the likelihood that Cr immobilisation at high loading involves poorly crystalline or compositionally heterogeneous domains that fall below the phase-resolution limits of PXRD.

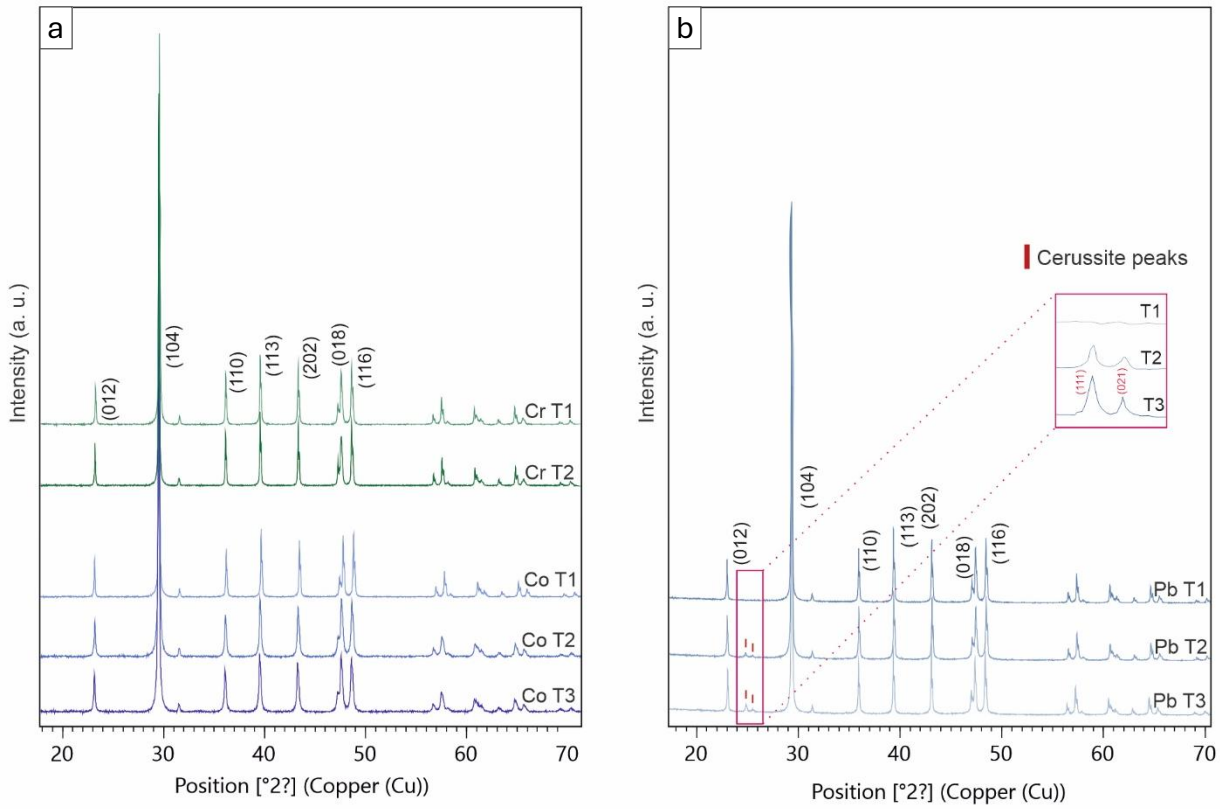

Figure 6. Stacked XRD patterns of Co, Cr and Pb treated samples (T1–T3). Patterns are vertically offset and normalised for visual comparison. In the Pb system (b), discrete cerussite reflections emerge at T2 and intensify at T3 (inset), whereas in c, Co treated samples remain calcite-dominated across all concentrations and Cr treated samples...

Table 1. **Table X.** Semi-quantitative phase proportions (wt%) from Rietveld refinement of PXRD data for Pb, Co and Cr treated samples (T1–T3).

Metal	Treatment	Calcite	Metal substituted calcite (≤5%)	Metal substituted calcite (5-10%)	Metal substituted calcite (10-15%)	Metal substituted calcite (15-20%)	Metal substituted calcite (20-25%)	Metal substituted calcite (25-30%)	Metal carbonate phases (e.g., cerussite, cobaltocalcite)	TOTAL
Pb	T1	98.33	1.46	<0.1	<0.1	<0.1	<0.1	<0.1	<0.1	99.79
	T2	71.39	23.32	2.18	<0.1	<0.1	<0.1	<0.1	3.18	100.07
	T3	68.19	24.78	1.57	<0.1	<0.1	<0.1	<0.1	6.21	100.75
Co	T1	23.3	72.5	4.9	<0.1	<0.1	<0.1	<0.1	N.A.	100.7
	T2	31.1	57.8	6.6	4.2	<0.1	<0.1	<0.1	N.A.	99.7
	T3	34.2	48.3	8.2	8.9	<0.1	<0.1	<0.1	N.A.	99.6
Cr	T1	17.3	26.6	56.8	N.A.	N.A.	N.A.	N.A.	N.A.	100.7
	T2	61.8	18.3	20.8	N.A.	N.A.	N.A.	N.A.	N.A.	100.9

3.4. Chemical composition and spatial partitioning of metals (SEM–EDS and µXRF)

Semi-quantitative SEM–EDS analyses and synchrotron µXRF mapping were used to constrain the chemical identity and spatial distribution of Pb-, Co- and Cr-bearing phases within the EICP precipitates. Representative EDS spectra and semi-quantitative compositional data for all treatments are provided in the Supplementary Materials. Because the EDS data are affected by matrix effects and multiphase interaction volumes,

they are interpreted in a comparative rather than fully quantitative sense, focusing on relative metal enrichment, co-association with Ca, and the presence or absence of anion signatures (C, S) indicative of carbonate versus sulphate or hydroxide phases. μXRF maps complement these spot analyses by resolving heterogeneous versus homogeneous metal distributions at the 2–5 μm scale, for Pb and Co.

3.4.1. Lead: distribution between Pb-substituted $CaCO_3$ and discrete Pb-carbonate phases

SEM–EDS analyses identify two chemically distinct carbonate domains across the Pb-treated samples. The first corresponds to Ca-rich carbonates containing variable amounts of Pb, consistent with Pb association within a $CaCO_3$ matrix. The second comprises Pb-rich carbonate domains characterised by high Pb contents coupled with very low Ca, which are chemically incompatible with Ca-rich carbonates containing Pb and are therefore interpreted as discrete Pb-carbonate phases.

At the highest Pb loading, T3, Pb-rich carbonate domains are abundant and well defined, with Pb contents typically ranging from approximately 22 to 48 wt% and Ca contents generally below about 9 wt%. These compositions are clearly distinct from those of Ca-rich carbonates and indicate a substantial expansion of the discrete Pb-carbonate population at high Pb availability. In T2, Pb-rich carbonate domains are present but less abundant, with Pb contents typically in the range of approximately 26 to 31 wt% and similarly low Ca contents. In contrast, in T1 such Pb-rich domains are very sparse, with only isolated analyses exceedingly approximately 30 wt% Pb, indicating that discrete Pb-carbonate precipitation is limited at low Pb loading.

In addition to point-based compositional analyses, backscattered electron imaging provides spatial context for the distribution of Pb-rich carbonate domains within the precipitates. In BSE images of T3 samples, Pb-rich domains are expressed as high-Z regions dispersed throughout an otherwise $CaCO_3$-dominated matrix (Fig. 7a). Binary segmentation of these high-Z regions highlights their heterogeneous spatial distribution and indicates that Pb-rich carbonate domains account for approximately 6–7% of the analysed area (Fig. 7b). Considered together with the phase assemblages identified by SEM–EDS and the semi-quantitative proportions obtained from Rietveld refinement; these observations provide independent and convergent evidence for the development of a discrete Pb-carbonate population at high Pb loading. The Pb-rich domains occur as spatially distinct entities embedded within a larger population of Ca-rich carbonate particles, rather than as a continuous solid solution or surface-enriched coating.

The dominant carbonate population in all treatments consists of Ca-rich carbonates containing lower and more variable Pb contents. In T3, Pb contents within Ca-rich carbonate domains range from below detection to approximately 9 wt%, with Ca remaining the dominant cation. A small number of analyses approach 10 wt% Pb, but higher values are rare. In T2, Ca-rich carbonate domains display a similar compositional range, with Pb contents typically between approximately 2 and 7 wt%. In T1, Pb-bearing

Ca-rich carbonates overwhelmingly dominate the assemblage, with Pb contents generally below 5 wt% and the majority of analyses falling below approximately 2 wt%.

In addition to bulk compositional differences, Ca-rich carbonate aggregates commonly exhibit internal chemical heterogeneity. SEM–EDS spot and μXRF mapping (Fig. 8c and e) analyses reveal Pb-enriched cores surrounded by Pb-depleted outer regions, producing concentric compositional zoning within individual carbonate particles rather than uniform Pb distribution throughout the carbonate mass. This intra-particle Pb partitioning is observed across all treatments and aggregate morphologies.

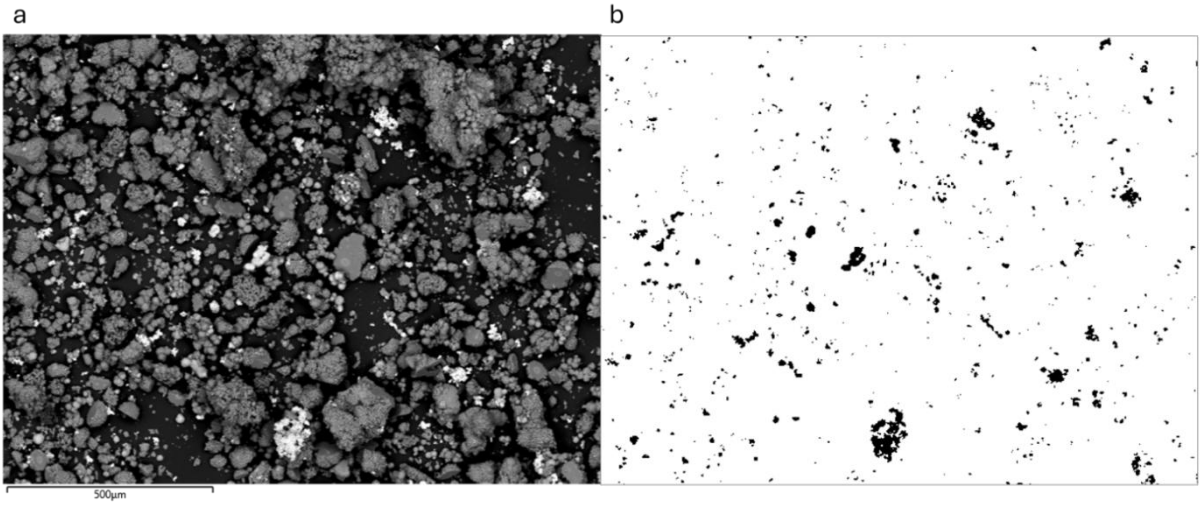

Figure 7. Backscattered electron (BSE) image of Pb-treated (T3) EICP precipitates (a, left) and corresponding binary segmentation mask of high-Z regions (b, right). Dark domains in the BSE image correspond to Pb-rich precipitates accounting for ~6–7% of the imaged area, which occur dispersed within a $CaCO_3$ dominated matrix (white).

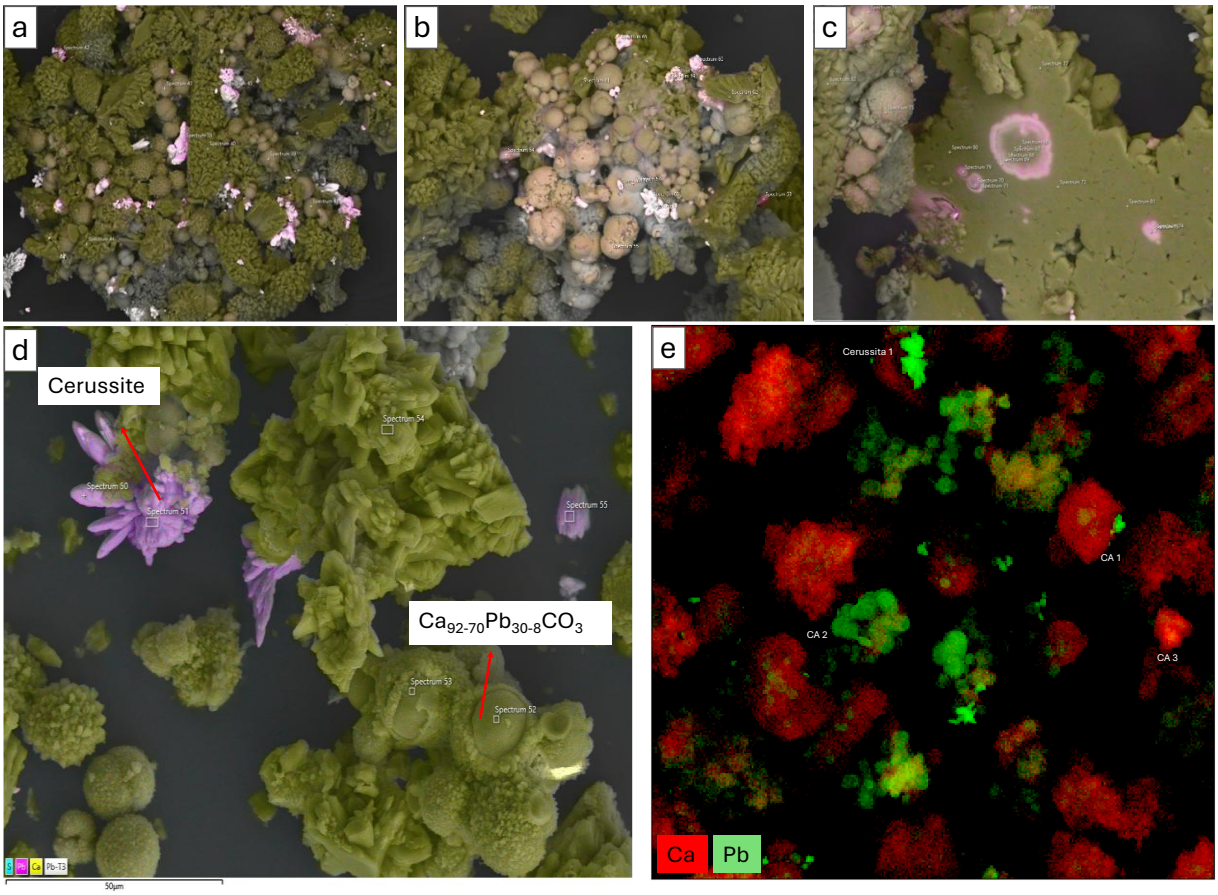

Figure 8. Representative SEM–EDS images of Pb-treated EICP precipitates showing the coexistence of Ca-rich carbonates and discrete Pb-carbonate phases. Bladed and fan-like crystals are assigned to cerussite, while surrounding aggregates are dominated by $CaCO_3$ with variable Pb contents. The nano-XRD map (right) resolves spatially discrete Pb-carbonate domains associated with, but crystallographically distinct from, the $CaCO_3$ framework. In addition, circular features within the centres of some carbonate aggregates correspond to Pb-enriched zones, as identified by spot EDS analyses and nano-XRD mapping.

3.4.2. Cobalt: diffuse enrichment and nanoscale overprinting of $CaCO_3$

Across all cobalt-treated systems, the precipitates are chemically dominated by Ca-rich carbonate, with cobalt occurring as a minor but detectable constituent distributed heterogeneously within the carbonate matrix. SEM–EDS analyses indicate that Co is consistently present at low absolute concentrations, with no evidence for the formation of discrete Co-rich carbonate phases in any treatment.

In T1, the vast majority of analysed points correspond to $CaCO_3$-rich domains containing only trace amounts of Co, typically below ~0.2 wt%, with occasional values approaching ~0.4 wt%. These Co-bearing carbonates are chemically indistinguishable from Ca-rich carbonate apart from the presence of minor Co, and no spatially discrete Co-enriched domains are observed. In T2, the overall chemical character remains Ca-dominated; however, the distribution of Co broadens slightly, with a small subset of analyses yielding Co contents up to ~0.7 wt%. Despite this modest increase, Co remains a minor component relative to Ca, and the data do not indicate the development of a chemically distinct Co-rich phase. In T3, the range of Co concentrations broadens

further, with maximum values locally reaching ~1.0–1.3 wt%. This increase reflects an enhanced capacity of the carbonate precipitates to accommodate Co under higher loading conditions, but Ca remains the dominant cation in all analysed domains. The Co-bearing carbonate compositions define a continuous spectrum rather than discrete compositional populations, suggesting diffuse Co incorporation or surface-associated enrichment rather than the nucleation of a separate cobalt carbonate phase.

Elemental maps obtained by SEM–EDS and μXRF further support this interpretation, showing Co signals broadly distributed across $CaCO_3$-rich aggregates without sharp internal boundaries, discrete Co-rich nuclei, or phase segregation at the micrometre scale. Local variations in Co intensity occur within individual particles but do not correspond to well-defined chemical domains.

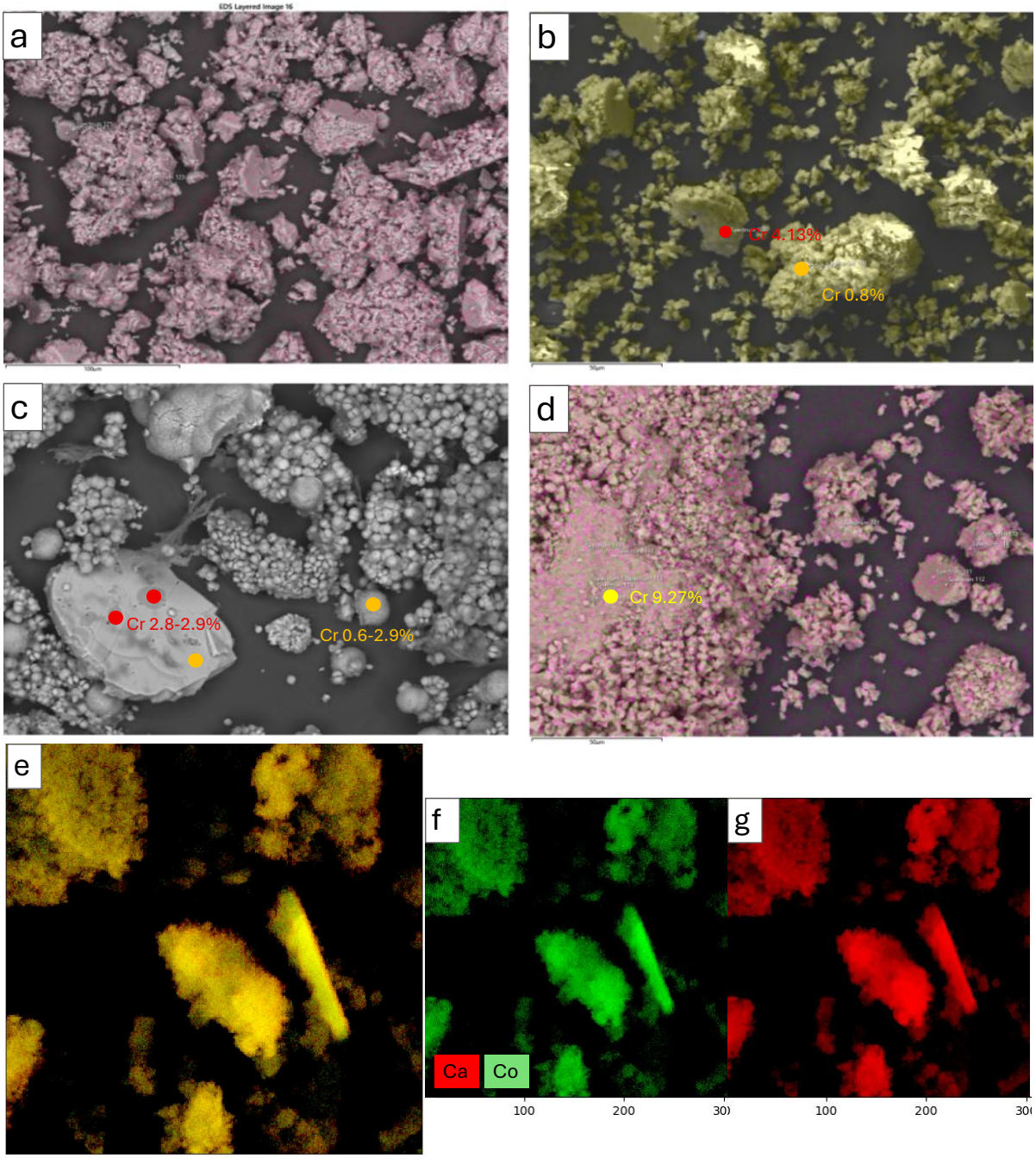

Figure 9. SEM–EDS images and elemental maps of Co-treated EICP precipitates. Carbonate aggregates exhibit typical globular to microcrystalline morphologies, with Co distributed broadly across $CaCO_3$ rich domains. No discrete Co-rich phases or sharply bounded Co-enriched domains are observed. Three-dimensional synchrotron nano-XRD mapping of Co-treated EICP precipitates. The reconstructed volumes show spatially consistent $CaCO_3$-dominated precipitates with Co-bearing signals distributed without pronounced internal variation. No discrete Co-rich domains or crystallographically distinct Co phases are resolved at the nanoscale.

3.4.3. Chromium: divergence from carbonate-dominated precipitation pathways

Across the Cr-treated systems, SEM–EDS analyses reveal a clear evolution in chemical partitioning with increasing Cr loading, marked by a transition from Ca-dominated carbonate compositions at low to intermediate concentrations to chemically distinct Cr-rich domains at the highest treatment level.

In CrT1, the precipitates are dominated by Ca-rich carbonate compositions, with Ca typically ranging between ~25 and 62 wt% and Cr occurring only at trace levels, generally below ~0.3 wt%. The majority of analysed points show Cr contents below ~0.2 wt%, with only rare spectra approaching ~0.3 wt%. These compositions are chemically consistent with $CaCO_3$-dominated carbonate phases bearing minor Cr, and no discrete Cr-rich domains are identified at this stage. Localised variations in Ca content occur, but Cr remains a minor component throughout the assemblage.

In CrT2, Ca-rich carbonate remains the dominant chemical component, but the distribution of Cr broadens modestly. Most analyses still yield Cr contents below ~0.5 wt%; however, a small number of spectra record elevated Cr concentrations reaching up to ~1 wt%. These higher values are spatially restricted and occur within otherwise Ca-dominated carbonate matrices. The data therefore suggest an increased association of Cr with carbonate phases at intermediate loading, while still preserving a chemically continuous spectrum rather than discrete Cr-rich phases.

In contrast, CrT3 exhibits a pronounced diversification in chemical compositions. Alongside Ca-rich carbonate domains similar to those observed in CrT1 and CrT2, a second population of analyses is characterised by markedly elevated Cr contents accompanied by reduced Ca. These Cr-rich domains show Cr concentrations commonly between ~1 and 10 wt%, and in several cases exceeding ~10 wt%, while Ca is strongly depleted or locally absent. Such compositions are chemically incompatible with simple Ca-rich carbonate and instead indicate the formation of Cr-dominated precipitates or mixed Cr-bearing phases distinct from the carbonate matrix.

The Cr-rich domains identified in CrT3 frequently coexist spatially with Ca-rich carbonate but form chemically discrete regions rather than representing a continuous compositional extension of the carbonate population. In several spectra, elevated Cr is accompanied by increased P and reduced Ca, suggesting a fundamental change in the dominant anionic framework relative to the carbonate-dominated assemblages observed at lower Cr loadings.

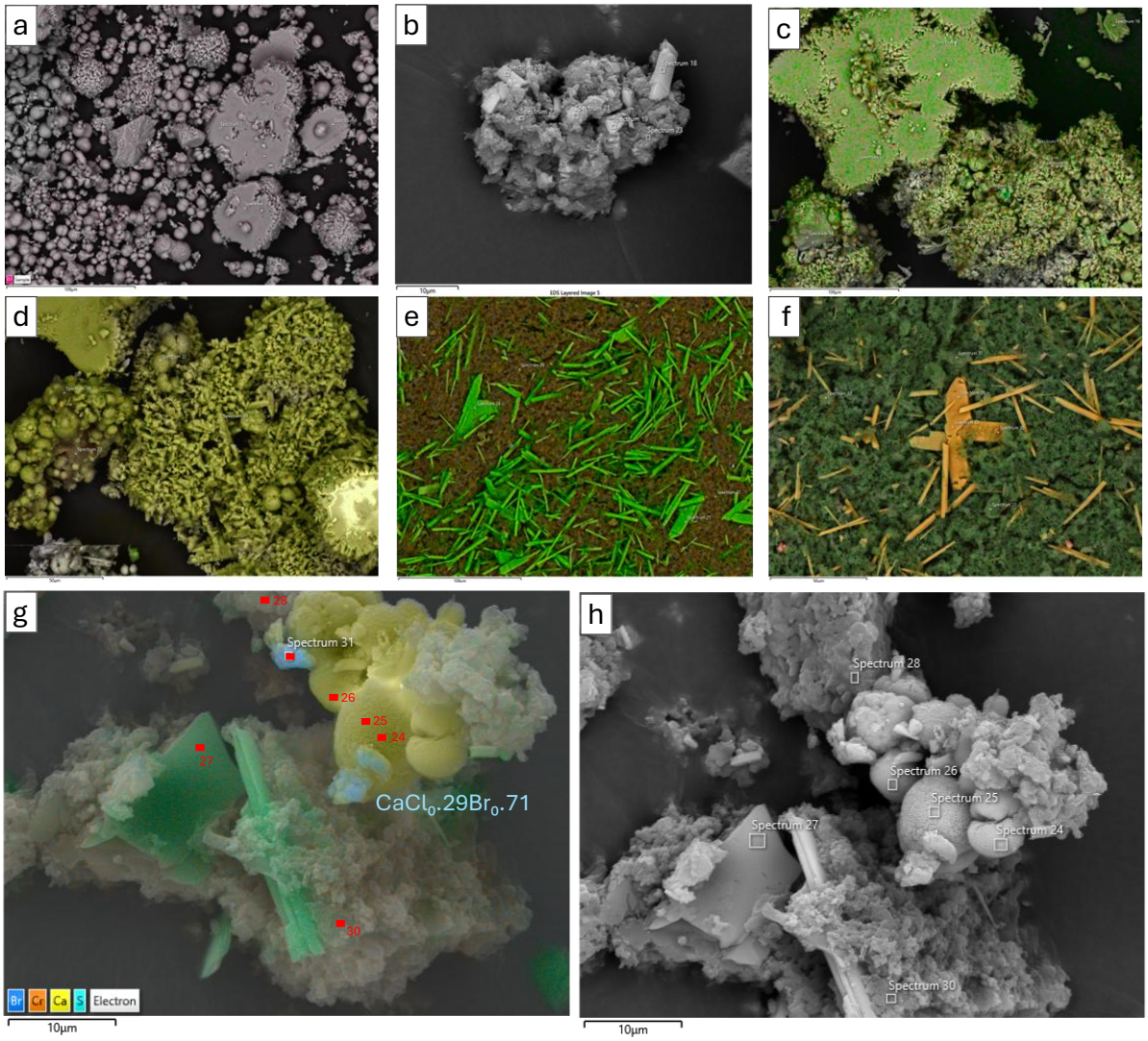

Figure 10. Enlarged SEM and SEM–EDS images of chromium-treated EICP precipitates showing the coexistence of carbonate-derived particles and non-carbonate Cr-rich assemblages, including fibrous, prismatic, and plate-like morphologies, together with halogen- and Ca-enriched domains identified by EDS.

4. Discussion

4. 1. Metal-specific crystallogenetic pathways in crude-enzyme EICP

The results indicate that, under otherwise identical crude-enzyme EICP conditions, Pb, Co and Cr follow distinct crystallogenetic trajectories that reflect differences in crystal-chemical compatibility, aqueous speciation, and interactions with evolving carbonate supersaturation. Rather than a single universal immobilisation mechanism, the data suggest that metal identity exerts first-order control over how carbonate precipitation pathways are modulated, which solid phases are stabilised and at what stage metal partitioning becomes effective.

Metal removal efficiencies reported here quantify short-term depletion of dissolved metals from solution but do not, on their own, resolve the mineralogical context or long-term stability of the retained metals. Distinguishing between operational removal and mineralogical immobilisation is therefore essential for interpreting the contrasting pathways observed across Pb, Co and Cr systems

In the Pb system, the observations are consistent with the behaviour expected for a lattice-compatible divalent metal with strong affinity for carbonate phases. At low to intermediate loadings, Pb is predominantly retained within $CaCO_3$-dominated assemblages at low substitution levels, while discrete cerussite becomes increasingly stabilised only as Pb availability rises. The dominance of the ≤5% substitution class and the absence of higher substitution levels suggest that calcite can accommodate Pb only to a limited extent before lattice strain and local supersaturation favour the nucleation of a Pb-dominated carbonate phase, as widely reported for Pb–calcite systems (Reeder, 1996; Sturchio et al., 1997; Reeder et al., 1999; Andersson et al., 2014). Microstructural and μXRF evidence further suggest that Pb partitioning is strongly stage-dependent, with pronounced enrichment within the cores of spherical and sunflower-like aggregates at low to intermediate loadings. This pattern indicates preferential Pb concentration during early precursor aggregation or initial crystallisation, prior to extensive $CaCO_3$ overgrowth, and is consistent with non-classical crystallisation pathways in which trace metals are incorporated into amorphous or poorly ordered carbonate precursors and subsequently diluted by later Ca-rich growth (Prieto et al., 2003; Mavromatis et al., 2017). As Pb loading increases, these early Pb-rich domains appear to act as loci for discrete cerussite stabilisation, leading to the coexistence of Pb-substituted calcite and $PbCO_3$ rather than a single homogeneous product. The Pb system therefore records a dual retention pathway combining early substitutional uptake with progressive phase segregation under higher metal activities.

Cobalt, by contrast, exhibits efficient immobilisation without evidence for the formation of a discrete cobalt carbonate phase across the investigated loading range. The dominance of Ca-rich carbonate and the continuous distribution of Co across low to moderate substitution classes suggest that Co is retained through diffuse incorporation and/or surface-associated enrichment rather than through nucleation of a Co-dominated mineral. This behaviour is consistent with cobalt's closer ionic-radius match to Ca^{2+} relative to Pb, but also with the strongly non-ideal nature of the $(Ca,Co)CO_3$ solid solution, which limits extensive lattice incorporation (Katsikopoulos et al., 2008). The decoupling between high Co removal efficiency and reduced precipitate mass further suggests that cobalt modifies carbonate growth kinetics rather than suppressing metal capture. Experimental and AFM studies show that Co^{2+} can perturb step propagation on calcite surfaces, stabilising early growth layers while inhibiting further advance, resulting in surface enrichment and sectoral overgrowth rather than deep solid-solution formation (Freij et al., 2004; Xu et al., 2015; Riechers et al., 2022). The filigree and vermicular morphologies observed in the present system are consistent with such adsorption-controlled growth regimes, indicating that cobalt is immobilised predominantly through

distributed nanoscale overprinting of $CaCO_3$ rather than through discrete phase segregation.

Chromium displays the strongest departure from carbonate-dominated behaviour, particularly at high loading, and this divergence coincides with pronounced changes in system-level conditions. At low to intermediate concentrations, Cr remains weakly associated with carbonate-dominated assemblages and occurs at low apparent substitution levels, consistent with the poor structural compatibility of Cr(III) with calcite and its strong tendency toward hydrolysis and aqueous complexation under alkaline conditions (Rai et al., 2007; Fang et al., 2022). At high loading, however, carbonate precipitation is strongly suppressed, and the system undergoes a fundamental shift away from carbonate-controlled mineralisation. SEM–EDS analyses reveal the emergence of chemically discrete Cr-rich domains characterised by elevated Cr and S and depleted Ca, which are incompatible with carbonate substitution or coprecipitation. The systematic association of Cr with S-bearing, Ca-poor domains, together with reduced ureolysis, lower carbonate yield and the collapse of calcite-dominated textures, indicates a redirection toward anion-controlled, non-carbonate immobilisation pathways. Although EDS does not permit definitive identification of sulphate minerals, the availability of sulphur introduced with the crude soybean extract and the $Cr_2(SO_4)_3$ reagent, combined with Cr-induced modification of aqueous chemistry, favours sequestration mechanisms that operate outside the carbonate stability field. Under these conditions, carbonate acts primarily as an early-stage or residual substrate, while Cr immobilisation proceeds predominantly via adsorption and surface precipitation within chemically distinct, non-carbonate domains. Similar redirection of mineralisation pathways has been reported in systems where trivalent metals disrupt carbonate supersaturation fields and promote alternative anion-controlled sinks (García-Sánchez & Alvarez-Ayuso, 2002; Scheinost et al., 2006; Islam et al., 2023).

4.2. Incidental immobilisation of non-target trace elements

Trace elements beyond the target metals were intermittently detected by SEM–EDS in a treatment-dependent manner, indicating minor co-association within the precipitate assemblages rather than the formation of additional dominant phases. In the chromium system, Hg was detected exclusively at the highest loading (Cr-T3) and only in a limited number of analysed spots, where it occurs at low wt% levels (approximately 0.5–2.2 wt%). Its absence from Cr-T1 and Cr-T2 indicates that Hg is not effectively incorporated or stabilised within carbonate-dominated assemblages. Instead, Hg occurrence in Cr-T3 is directly associated with the pronounced mineralogical transition observed at this loading, where carbonate precipitation is replaced by sulphate-rich phases. These non-carbonate solids are inferred to provide more permissive structural environments or surface binding sites for Hg retention, enabling its local stabilisation at levels resolvable by EDS.

Copper was also detected sporadically across treatments at low wt% levels. In the Cr system, Cu occurs primarily in Cr-T3 (approximately 0.8–3.7 wt%) and more locally

in individual spots from Cr-T2 (~0.9 wt%) and Cr-T1 (~1.1 wt%), consistent with heterogeneous uptake at the aggregate scale. In the Pb system, Cu was likewise detected as a minor component in Pb-T3 at similarly low levels and in a spot-specific manner, rather than as a pervasive signal across the $CaCO_3$-rich matrix.

Taken together, these observations indicate that trace Cu and Hg are not introduced as external contaminants but are instead present at low background levels, plausibly originating from the crude soybean extract used in enzyme preparation. Their detection reflects selective stabilisation or retention within specific microdomains, particularly under conditions where carbonate precipitation is suppressed or replaced by alternative mineral phases. These trace associations are therefore interpreted as secondary immobilisation processes occurring within chemically distinct domains resolved by the SEM–EDS interaction volume, rather than as evidence for discrete Cu- or Hg-bearing mineral phases.

4.3. Sunflower-like textures as a shared morphological motif with metal-dependent expression

Sunflower-like carbonate aggregates occur systematically across Pb, Co and Cr treated systems and represent a recurring morphological outcome of crude-enzyme EICP rather than a metal-specific phase. Their repeated appearance across chemically distinct treatments indicates that these structures arise from a shared crystallogenetic pathway intrinsic to the enzyme-driven carbonate system, upon which metal identity and loading exert secondary, modulatory effects. A plausible mechanistic framework for this behaviour is provided by non-classical models of $CaCO_3$ mineralisation, in which solute prenucleation clusters undergo liquid–liquid phase separation to form nanodroplets of a dense liquid precursor that subsequently aggregate, coalesce and solidify into amorphous or poorly ordered calcium carbonate (Gebauer et al., 2008; Avaro et al., 2019; Gindele et al., 2024).

Within this framework, sunflower-like textures are interpreted to originate from the aggregation and partial coalescence of nanoscale liquid or amorphous precursor domains formed under conditions of rapid carbonate supersaturation induced by ureolysis. Colloidal stabilisation by organic components inherited from the crude enzyme extract likely promotes imperfect coalescence of these precursor droplets, enabling the internalisation of former droplet interfaces and associated chemical heterogeneities. Upon progressive dehydration and solidification, these precursor bodies undergo crystallisation, producing radially organised, fan-like or petal-shaped crystalline units propagating outward from a central nucleus (Fig. 7, steps 1 and 2). Such radial architectures are consistent with growth under diffusion-limited conditions, where local gradients in carbonate activity, calcium availability and organic ligands inherited from the precursor phase govern crystallisation directionality (Fig. 7, steps 3 to 6) (Gower, 2008; Gindele et al., 2024).

Metal presence does not appear to dictate the formation of the sunflower morphology itself but strongly influences its internal chemical architecture and

expression. In Pb and Cr treated systems, sunflower-like units are commonly embedded within larger composite aggregates, suggesting early nucleation followed by subsequent overgrowth and aggregation. Compositional mapping reveals that these structures frequently host metal-enriched cores, particularly in the Pb system, indicating that they act as preferential loci for early-stage metal association during precursor formation or initial solidification. This core-enrichment pattern implies that metal uptake is most efficient during the earliest stages of aggregate development, prior to full crystallographic ordering and before subsequent $CaCO_3$ overgrowth progressively dilutes metal concentrations towards aggregate margins. Such behaviour is consistent with metal partitioning into metastable, chemically heterogeneous precursor environments rather than substitution into a fully ordered calcite lattice (De Yoreo et al., 2015; Gindele et al., 2024).

In contrast, Co-treated systems preserve sunflower-like particles alongside filigree and vermicular textures, reflecting a broader morphological spectrum consistent with more diffuse metal association and weaker perturbation of the carbonate growth field. The absence of discrete Co-rich domains and the predominance of Ca-rich carbonate across these aggregates suggest that cobalt primarily influences growth kinetics and texture development without strongly partitioning into specific structural loci, in line with its more limited affinity for early-stage carbonate precursors relative to Pb and Cr.

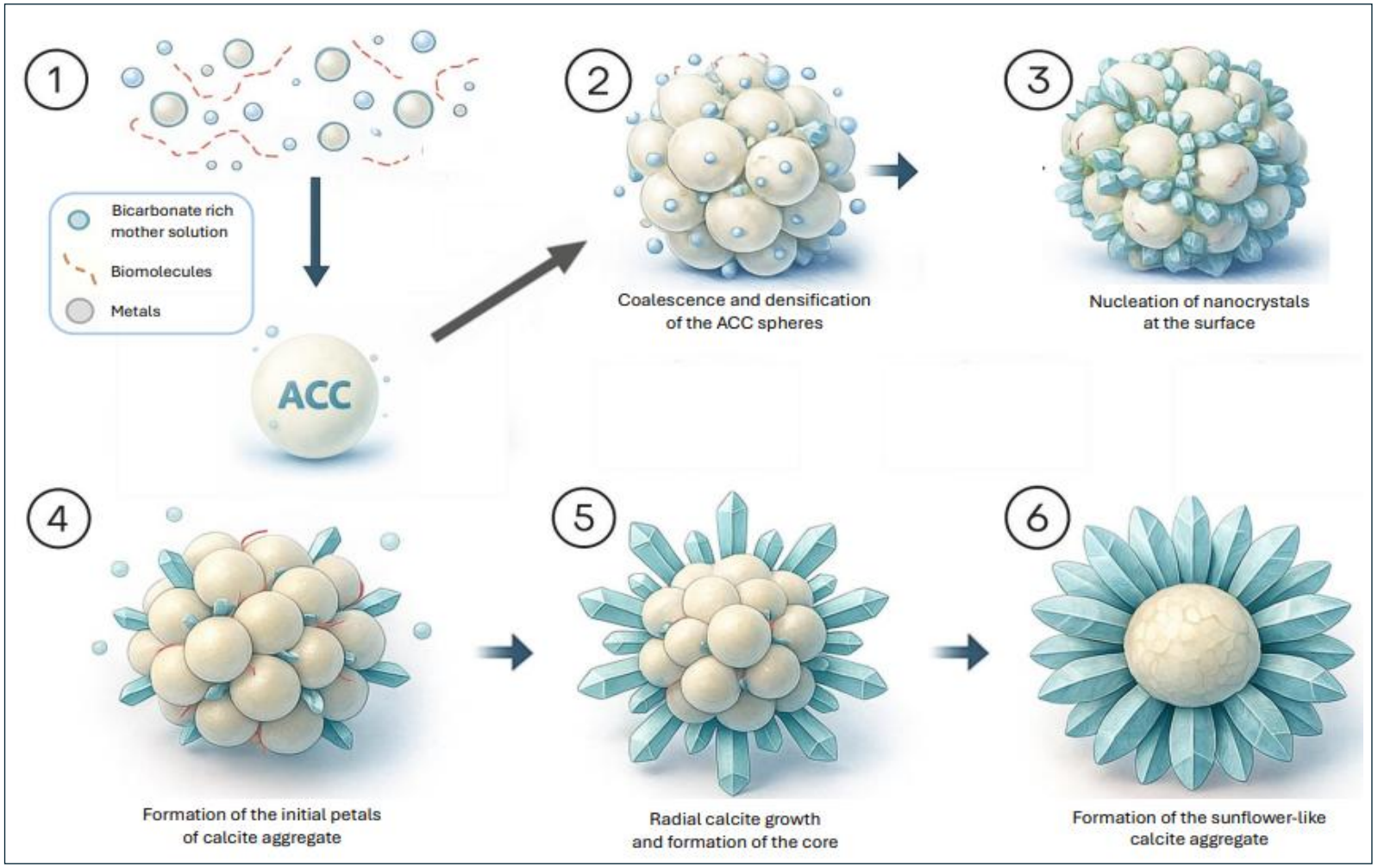

Figure 7. *Crystallogenetic pathway leading to the formation of sunflower-like calcite aggregates.* (1) In a bicarbonate-rich mother solution, biomolecules interact with dissolved ions and metals forming biomolecule-stabilised ACC precursor (2) Amorphous calcium carbonate (ACC) spheres form and undergo coalescence and densification. (3) Nanocrystal nucleation initiates at the ACC surface. (4) Outward growth of the first calcite petals begins. (5) Radial calcite development continues, generating a structured core. (6) Final formation of the sunflower-like calcite aggregate, characterised by an inner consolidated core surrounded by radially organised calcite crystals.

Conclusions

Crude-enzyme EICP does not yield a single, calcite-dominated immobilisation outcome; instead, it accesses a spectrum of metal-specific mineralisation pathways that determine how, and how effectively, metals are retained. Across all treatments, carbonate precipitation is initiated under conditions of ureolysis-driven supersaturation, giving rise to a shared amorphous or liquid-like precursor stage that acts as a common morphological and chemical template. The recurrent development of sunflower-like aggregates across Pb, Co and Cr T1 and T2 treated systems reflects this precursor-controlled pathway rather than the formation of metal-specific mineral phases.

Within this common framework, metal identity and loading exert strong control over the internal architecture, mineralogical trajectory, and immobilisation mechanism of the resulting precipitates. In the Pb system, increasing metal loading promotes a transition from dispersed Pb association within $CaCO_3$-dominated assemblages to the formation of discrete Pb-rich carbonate domains, indicating a shift from restricted incorporation to phase segregation at higher concentrations. In contrast, Co is efficiently immobilised across all treatments without detectable formation of a discrete cobalt carbonate phase, consistent with diffuse association within calcite-dominated products and a limited perturbation of the underlying crystallisation pathway.

The Cr system exhibits a fundamentally different behaviour. At high loading, mineralisation shifts away from carbonate-dominated precipitation towards non-carbonate, anion-controlled Cr-rich domains, reflecting the strong hydrolysis behaviour of trivalent chromium and the decisive influence of counter-ion chemistry. This transition governs Cr immobilisation and generates mineralogical environments capable of locally stabilising additional trace elements. The selective detection of Hg and Cu in Cr-T3, and Cu in Pb-T3, indicates that trace metals present at low background levels, likely introduced with the crude enzyme extract, are not uniformly incorporated during carbonate precipitation but can be retained within chemically distinct microdomains under specific mineralogical conditions.

Importantly, sunflower-like aggregates emerge as a microstructural record of early-stage crystallisation rather than a discrete mineralogical phase. Their radial organisation and frequent association with metal-enriched cores indicate that metal uptake is most efficient during the earliest stages of precursor aggregation and destabilisation, prior to full crystallographic ordering and subsequent $CaCO_3$ overgrowth. Metal identity therefore modulates how this shared morphological template is expressed, imprinting chemically distinct internal architectures onto an otherwise common structural motif.

Taken together, these findings demonstrate that EICP-driven remediation cannot be reduced to calcite formation alone. Instead, effective, and durable metal immobilisation depends on how enzymatically generated supersaturation, organic mediation from crude extracts and metal-specific aqueous chemistry interact to select mineralogical pathways. From an applied perspective, remediation strategies should therefore be designed with explicit consideration of metal identity, loading thresholds

and the broader ionic environment, particularly for systems involving hydrolysing multivalent metals or mixed contaminant suites.

References

Abdel-Gawwad, H. A., Hussein, Hala. S., & Mohammed, M. S. (2020). Bio-removal of Pb, Cu, and Ni from solutions as nano-carbonates using a plant-derived urease enzyme–urea mixture. *Environmental Science and Pollution Research*, *27*(24), 30741–30754. https://doi.org/10.1007/s11356-020-09359-y

Achal, V., & Pan, X. (2014). Influence of Calcium Sources on Microbially Induced Calcium Carbonate Precipitation by Bacillus sp. CR2. *Applied Biochemistry and Biotechnology*, *173*(1), 307–317. https://doi.org/10.1007/s12010-014-0842-1

Addadi, L., & Weiner, S. (1985). Interactions between acidic proteins and crystals: stereochemical requirements in biomineralization. *Proceedings of the National Academy of Sciences*, *82*(12), 4110–4114. https://doi.org/10.1073/pnas.82.12.4110

Ahenkorah, I., Rahman, M. M., Karim, M. R., Beecham, S., & Saint, C. (2021). A Review of Enzyme Induced Carbonate Precipitation (EICP): The Role of Enzyme Kinetics. In *Sustainable Chemistry* (Vol. 2, Issue 1, pp. 92–114). Multidisciplinary Digital Publishing Institute (MDPI). https://doi.org/10.3390/suschem2010007

Amjad, Z. (1999). Precipitation of calcium carbonate in aqueous systems; the influence of natural and synthetic polyelectrolytes. *Tenside Surfactants Detergents*, *36*(3), 162–167. https://doi.org/10.1515/tsd-1999-360305

Amjad, Z. (2006). Influence of natural and synthetic additives on calcium carbonate precipitation and crystal morphology. *Tenside Surfactants & Detergents*, 43(4), 184-191. https://doi.org/10.3139/113.100306

Andersson, M. P., Sakuma, H., & Stipp, S. L. S. (2014). Strontium, Nickel, Cadmium, and Lead Substitution into Calcite, Studied by Density Functional Theory. *Langmuir*, *30*(21), 6129–6133. https://doi.org/10.1021/la500832u

Baffoe, E., & Ghahremaninezhad, A. (2022). The effect of biomolecules on enzyme-induced calcium carbonate precipitation in cementitious materials. *Construction and Building Materials*, *345*. https://doi.org/10.1016/j.conbuildmat.2022.128323

Bian, Y., Chen, Y., Zhan, L., Ke, H., Gao, Y., Wang, Q., & Qi, G. (2024). An Enzyme-Induced Carbonate Precipitation Method for Zn2+, Ni2+, and Cr(VI) Remediation: An Experimental and Simulation Study. *Applied Sciences (Switzerland)*, *14*(15). https://doi.org/10.3390/app14156559

Callagon, E., Fenter, P., Nagy, K. L., & Sturchio, N. C. (2014). Incorporation of Pb at the Calcite (104)–Water Interface. *Environmental Science & Technology*, *48*(16), 9263–9269. https://doi.org/10.1021/es5014888

Callagon, E. B. R., Lee, S. S., Eng, P. J., Laanait, N., Sturchio, N. C., Nagy, K. L., & Fenter, P. (2017). Heteroepitaxial growth of cadmium carbonate at dolomite and calcite surfaces: Mechanisms and rates. *Geochimica et Cosmochimica Acta*, *205*, 360–380. https://doi.org/10.1016/j.gca.2016.12.007

Caulfield, B., Roberts, M., & Prigiobbe, V. (2023). Studying the effect of nickel, copper, and zinc on the precipitation kinetics and the composition of Ca-carbonates for the integrated process of CO_2 mineralization and brine mining. *Chemical Engineering Journal, 476*, 146220. https://doi.org/10.1016/j.cej.2023.146220

Chen, Y., Wang, Q., Bian, Y., Zhan, L., Gao, Y., Guo, H., Wang, Y., & Gao, Y. (2024). Effects of enzyme-induced carbonate precipitation (EICP) with different urease sources on the zinc remediation. *Journal of Hazardous Materials*, *480*. https://doi.org/10.1016/j.jhazmat.2024.136321

Chen, Y., Bian, Y., Zhan, L., Wang, Y., Gao, Y., & Wang, L. (2025). Effects of multi-source plant-derived urease enzyme on the morphology, growth, size, and distribution behavior of calcium carbonate through enzyme-induced carbonate precipitation method: a microfluidic chip experiment. *Acta Geotechnica*. https://doi.org/10.1007/s11440-025-02586-y

Davis, J. A., Fuller, C. C., & Cook, A. D. (1987). A model for trace metal sorption processes at the calcite surface: Adsorption of Cd*+ and subsequent solid solution formation. *Geochimica et Cosmochimica Acta*, *51*.

Demichelis, R., Raiteri, P., Gale, J. D., Quigley, D., & Gebauer, D. (2011). Stable prenucleation mineral clusters are liquid-like ionic polymers. *Nature Communications*, *2*(1), 590. https://doi.org/10.1038/ncomms1604

de Yoreo, J. J. (2003). Principles of Crystal Nucleation and Growth. *Reviews in Mineralogy and Geochemistry*, *54*(1), 57–93. https://doi.org/10.2113/0540057

Dickinson, H., MacDonald, J., & Toney, J. L. (2025). Enzyme-mediated multiphase precipitation: An innovative strategy for ecotoxic metal immobilization in aqueous systems. *Journal of Environmental Chemical Engineering*, *13*(5), 119087. https://doi.org/10.1016/j.jece.2025.119087

Doebelin, N., & Kleeberg, R. (2015). *Profex* : a graphical user interface for the Rietveld refinement program *BGMN*. *Journal of Applied Crystallography*, *48*(5), 1573–1580. https://doi.org/10.1107/S1600576715014685

Elzinga, E. J., & Reeder, R. J. (2002). X-ray absorption spectroscopy study of Cu2+ and Zn2+ adsorption complexes at the calcite surface. *Geochimica et Cosmochimica Acta*, *66*(22), 3943–3954. https://doi.org/10.1016/S0016-7037(02)00971-7

Elzinga, E. J., Rouff, A. A., & Reeder, R. J. (2006). The long-term fate of Cu2+, Zn2+, and Pb2+ adsorption complexes at the calcite surface: An X-ray absorption spectroscopy study. *Geochimica et Cosmochimica Acta*, *70*(11), 2715–2725. https://doi.org/10.1016/j.gca.2006.02.026

Fang, Z., Liu, W., Yao, T., Zhou, G., Wei, S., & Qin, L. (2022). Experimental study of chromium (III) coprecipitation with calcium carbonate. *Geochimica et Cosmochimica Acta*, *322*, 94–108. https://doi.org/10.1016/j.gca.2022.01.019

Fernández-Martínez, A., Román-Ross, G., Cuello, G. J., Turrillas, X., Charlet, L., Johnson, M. R., & Bardelli, F. (2006). Arsenic uptake by gypsum and calcite: Modelling and probing by neutron and X-ray scattering. *Physica B: Condensed Matter*, *385–386*, 935–937. https://doi.org/10.1016/j.physb.2006.05.276

Freij, S. J., Putnis, A., & Astilleros, J. M. (2004). Nanoscale observations of the effect of cobalt on calcite growth and dissolution. *Journal of Crystal Growth*, *267*(1–2), 288–300. https://doi.org/10.1016/j.jcrysgro.2004.03.044

García-Sánchez, A., & Álvarez-Ayuso, E. (2002). Sorption of Zn, Cd and Cr on calcite. Application to purification of industrial wastewaters. *Minerals Engineering*, *15*(7), 539–547. https://doi.org/10.1016/S0892-6875(02)00072-9

Gebauer, D., Völkel, A., & Cölfen, H. (2008). Stable Prenucleation Calcium Carbonate Clusters. *Science*, *322*(5909), 1819–1822. https://doi.org/10.1126/science.1164271

Gilmour, K. A., Ghimire, P. S., Wright, J., Haystead, J., Dade-Robertson, M., Zhang, M., & James, P. (2024). Microbially induced calcium carbonate precipitation through CO2 sequestration via an engineered Bacillus subtilis. *Microbial Cell Factories*, *23*(1), 168. https://doi.org/10.1186/s12934-024-02437-7

González-López, J., Ruiz-Hernández, S. E., Fernández-González, Á., Jiménez, A., de Leeuw, N. H., & Grau-Crespo, R. (2014). Cobalt incorporation in calcite: Thermochemistry of (Ca,Co)CO 3 solid solutions from density functional theory simulations. *Geochimica et Cosmochimica Acta*, *142*, 205–216. https://doi.org/10.1016/j.gca.2014.07.026

Gower, L. B. (2008). Biomimetic model systems for investigating the amorphous precursor pathway and its role in biomineralization. *Chemical Reviews*, *108*(11), 4551–4627. https://doi.org/10.1021/cr800443h

Hemayati, M., Aghaei, H., Daman Shokouh, A., Nikooee, E., Niazi, A., & Khodadadi Tirkolaei, H. (2024). A pore-scale study of fracture sealing through enzymatically-induced carbonate precipitation (EICP) method demonstrates its potential for CO2 storage management. *Scientific Reports*, *14*(1), 17832. https://doi.org/10.1038/s41598-024-68720-0

Henderson, G. E., Murray, B. J., & McGrath, K. M. (2008). Controlled variation of calcite morphology using simple carboxylic acids. *Journal of Crystal Growth*, *310*(18), 4190–4198. https://doi.org/10.1016/j.jcrysgro.2008.07.002

Kim, J. J., Lee, S. S., Fenter, P., Myneni, S. C. B., Nikitin, V., & Peters, C. A. (2023). Carbonate Coprecipitation for Cd and Zn Treatment and Evaluation of Heavy Metal Stability Under Acidic Conditions. *Environmental Science & Technology*, *57*(8), 3104–3113. https://doi.org/10.1021/acs.est.2c07678

Lakshtanov, L. Z., & Stipp, S. L. S. (2007). Experimental study of nickel(II) interaction with calcite: Adsorption and coprecipitation. *Geochimica et Cosmochimica Acta*, *71*(15), 3686–3697. https://doi.org/10.1016/j.gca.2007.04.006

Lee, Y. J., Elzinga, E. J., & Reeder, R. J. (2005). Cu(II) adsorption at the calcite–water interface in the presence of natural organic matter: Kinetic studies and molecular-scale characterization. *Geochimica et Cosmochimica Acta*, *69*(1), 49–61. https://doi.org/10.1016/j.gca.2004.06.015

Lee, H. H. (2025). Adsorption characteristics of cadmium onto calcite and its agricultural environmental relevance. *Heliyon*, *11*(1). https://doi.org/10.1016/j.heliyon.2024.e40241

Li, W., Zhang, Y., & Achal, V. (2022). Mechanisms of cadmium retention on enzyme-induced carbonate precipitation (EICP) of Ca/Mg: Nucleation, chemisorption, and co-precipitation. *Journal of Environmental Chemical Engineering*, *10*(3). https://doi.org/10.1016/j.jece.2022.107507

Ma, C., Xu, F., Zhu, Z., Yang, H., Nong, P., Kang, Z., Tang, S., Zhang, L., & Zhu, Y. (2022). Dissolution and Solubility of the Calcite–Otavite Solid Solutions [(Ca1−x Cdx)CO3] at 2° C. *Minerals*, *12*(6). https://doi.org/10.3390/min12060756

McBride, M. B. (1980). Chemisorption of Cd2+ on Calcite Surfaces. *Soil Science Society of America Journal*, *44*(1), 26–28. https://doi.org/10.2136/sssaj1980.03615995004400010006x

Morse, J. W., Arvidson, R. S., & Lüttge, A. (2007). Calcium Carbonate Formation and Dissolution. *Chemical Reviews*, *107*(2), 342–381. https://doi.org/10.1021/cr050358j

Naka, K., & Chujo, Y. (2001). Control of Crystal Nucleation and Growth of Calcium Carbonate by Synthetic Substrates. *Chemistry of Materials*, *13*(10), 3245–3259. https://doi.org/10.1021/cm011035g

Okumura, M., & Kitano, Y. (1986). Coprecipitation of alkali metal ions with calcium carbonate. *Geochimica et Cosmochimica Acta*, *50*(1), 49–58. https://doi.org/10.1016/0016-7037(86)90047-5

Orme CA, Noy A, Wierzbicki A, McBride MT, Grantham M, Teng HH, Dove PM, DeYoreo JJ. Formation of chiral morphologies through selective binding of amino acids to calcite

surface steps. Nature. 2001 Jun 14;411(6839):775-9. doi: 10.1038/35081034. PMID: 11459051

Papadopoulos, P., & Rowell, D. L. (1988). The reactions of cadmium with calcium carbonate surfaces. *Journal of Soil Science*, *39*(1), 23–36. https://doi.org/10.1111/j.1365-2389.1988.tb01191.x

Pastero, L., Costa, E., Bruno, M., Rubbo, M., Sgualdino, G., & Aquilano, D. (2004). Morphology of Calcite ($CaCO_3$) Crystals Growing from Aqueous Solutions in the Presence of Li^+ Ions. Surface Behavior of the {0001} Form. *Crystal Growth & Design*, *4*(3), 485–490. https://doi.org/10.1021/cg034217r

Parsiegla, K. I., & L. Katz, J. (2000). Calcite growth inhibition by copper(II). *Journal of Crystal Growth*, *213*(3–4), 368–380. https://doi.org/10.1016/S0022-0248(00)00306-7

Putnis, A., & Putnis, C. v. (2007). The mechanism of reequilibration of solids in the presence of a fluid phase. *Journal of Solid State Chemistry*, *180*(5), 1783–1786. https://doi.org/10.1016/j.jssc.2007.03.023

Rai, D., Moore, D. A., Hess, N. J., Rosso, K. M., Rao, L., & Heald, S. M. (2007). Chromium(III) hydroxide solubility in the aqueous K+-H +-OH--CO2-HCO 3- -CO 32- -H2O system: A thermodynamic model. *Journal of Solution Chemistry*, *36*(10), 1261–1285. https://doi.org/10.1007/s10953-007-9179-5

Rajasekar, A., Omoregie, A. I., & Kui, K. F. (2025). Urease-catalyzed microbial and enzymatic carbonate precipitation for eco-friendly heavy metal remediation. In *Letters in Applied Microbiology* (Vol. 78, Issue 2). Oxford University Press. https://doi.org/10.1093/lambio/ovaf022

Reeder, R. J. (1996). Interaction of divalent cobalt, zinc, cadmium, and barium with the calcite surface during layer growth. In *Pergamon Geochimica et Cosmochimica Acta* (Vol. 60, Issue 9).

Reeder, R. J., Lamble, G. M., & Northrup, P. A. (1999). XAFS study of the coordination and local relaxation around Co 2+ , Zn 2+ , Pb 2+ , and Ba 2+ trace elements in calcite BACKGROUND AND SCOPE. In *American Mineralogist* (Vol. 84).

Renard, F., Putnis, C. v., Montes-Hernandez, G., Ruiz-Agudo, E., Hovelmann, J., & Sarret, G. (2015). Interactions of arsenic with calcite surfaces revealed by in situ nanoscale imaging. *Geochimica et Cosmochimica Acta*, *159*, 61–79. https://doi.org/10.1016/j.gca.2015.03.025

Riechers, S. L., Ilton, E. S., Qafoku, O., Du, Y., & Kerisit, S. N. (2022). Cobalt hydroxide–cobalt carbonate competitive growth on carbonate surfaces. *Chemical Geology*, *605*. https://doi.org/10.1016/j.chemgeo.2022.120951

Rodriguez-Navarro, C., Kudłacz, K., Cizer, Ö., & Ruiz-Agudo, E. (2015). Formation of amorphous calcium carbonate and its transformation into mesostructured calcite. *CrystEngComm*, *17*(1), 58–72. https://doi.org/10.1039/C4CE01562B

Rouff, A. A., Reeder, R. J., & Fisher, N. S. (2002). Pb (II) Sorption with Calcite: A Radiotracer Study. In *Aquatic Geochemistry* (Vol. 8).

Saif, A., Cuccurullo, A., Gallipoli, D., Perlot, C., & Bruno, A. W. (2022). Advances in Enzyme Induced Carbonate Precipitation and Application to Soil Improvement: A Review. In *Materials* (Vol. 15, Issue 3). MDPI. https://doi.org/10.3390/ma15030950

Sikirić, M. D., & Füredi-Milhofer, H. (2006). The influence of surface active molecules on the crystallization of biominerals in solution. *Advances in Colloid and Interface Science*, *128–130*, 135–158. https://doi.org/10.1016/j.cis.2006.11.022

Shu, S., Yan, B., Ge, B., Li, S., & Meng, H. (2022). Factors Affecting Soybean Crude Urease Extraction and Biocementation via Enzyme-Induced Carbonate Precipitation (EICP) for Soil Improvement. *Energies*, *15*(15). https://doi.org/10.3390/en15155566

Stipp, S. L., Hochella, M. F., Park&~, G. A., & Leckie', J. 0. (1992). Cd*+ uptake by caicite, solid-state diffusion, and the formation of solid-solution: Interface processes observed with near-surface sensitive techniques (XI'S, LEED, and AES). In *Geochimica ef Cosmochimica Acfa* (Vol. 56).

Sturchio, N. C., Chiarello, R. P., Cheng, L., Lyman, P. F., Bedzyk, M. J., Qian, Y., You, H., Yee, D., Geissbuhler, P., Sorensen, L. B., Liang, Y., & Baer, D. R. (1997). Lead adsorption at the calcite-water interface: Synchrotron X-ray standing wave and X-ray reflectivity studies. *Geochimica et Cosmochimica Acta*, *61*(2), 251–263. https://doi.org/10.1016/S0016-7037(96)00326-2

United Nations Environment Programme (UNEP) (2021) Food Waste Index Report 2021. Nairobi. 2021 United Nations Environment Programme. https://www.unep.org/resources/report/unep-food-waste-index-report-2021

Wada, N., Kanamura, K., & Umegaki, T. (2001). Effects of carboxylic acids on the crystallization of calcium carbonate. *Journal of Colloid and Interface Science*, *233*(1), 65–72. https://doi.org/10.1006/jcis.2000.7215

Wang, L., Cheng, W.-C., & Xue, Z.-F. (2022a). The Effect of Calcium Source on Pb and Cu Remediation Using Enzyme-Induced Carbonate Precipitation. *Frontiers in Bioengineering and Biotechnology*, *10*. https://doi.org/10.3389/fbioe.2022.849631

Wang, L., Cheng, W. C., Xue, Z. F., & Hu, W. (2022b). Effects of the Urease Concentration and Calcium Source on Enzyme-Induced Carbonate Precipitation for Lead Remediation. *Frontiers in Chemistry*, *10*. https://doi.org/10.3389/fchem.2022.892090

Wang, L., Cheng, W. C., Xue, Z. F., Zhang, B., & Lv, X. J. (2023). Immobilizing of lead and copper using chitosan-assisted enzyme-induced carbonate precipitation. *Environmental Pollution*, *319*. https://doi.org/10.1016/j.envpol.2022.120947

Weiner, S., & Addadi, L. (2011). Crystallization Pathways in Biomineralization. *Annual Review of Materials Research*, *41*(1), 21–40. https://doi.org/10.1146/annurev-matsci-062910-095803

Wu, Q., Huang, Y., Irga, P., Kumar, P., Li, W., Wei, W., Shon, H. K., Lei, C., & Zhou, J. L. (2024). Synergistic control of urban heat island and urban pollution island effects using green infrastructure. In *Journal of Environmental Management* (Vol. 370). Academic Press. https://doi.org/10.1016/j.jenvman.2024.122985

Xu, M., Ilton, E. S., Engelhard, M. H., Qafoku, O., Felmy, A. R., Rosso, K. M., & Kerisit, S. (2015). Heterogeneous growth of cadmium and cobalt carbonate phases at the calcite {10$\bar{1}$4} surface. *Chemical Geology, 397*, 24–36. https://doi.org/10.1016/j.chemgeo.2015.01.003

Xu, W., Zheng, J., Cui, M., & Lai, H. (2025). Enzyme-Induced Carbonate Precipitation for the Stabilization of Heavy Metal-Contaminated Landfill Soils: A Sustainable Approach to Resource Recovery and Environmental Remediation. *Sustainability (Switzerland)*, *17*(10). https://doi.org/10.3390/su17104630

Zeng, H., Jin, B., Xu, S., Han, L., Wang, J., Jia, H., Dapaah, M. F., & Cheng, L. (2025). Removal of copper, lead and cadmium from water through enzyme-induced carbonate precipitation by soybean urease. *Environmental Research*, *277*. https://doi.org/10.1016/j.envres.2025.121610

Zhizhaev, A. M., & Merkulova, E. N. (2014). Interaction of copper(II) and zinc(II) in coprecipitation from sulfate solutions with natural calcium carbonate. *Russian Journal of Applied Chemistry*, *87*(1), 16–22. https://doi.org/10.1134/S1070427214010029